Exploring the active galactic nucleus and starburst content of local ultraluminous infrared galaxies through 5–8 μm spectroscopy

E. Nardini,[1]★ G. Risaliti,[2,3] M. Salvati,[2] E. Sani,[1] Y. Watabe,[2] A. Marconi[1] and R. Maiolino[4]

[1]*Dipartimento di Astronomia e Scienza dello Spazio, Università di Firenze, L.go E. Fermi 2, 50125 Firenze, Italy*
[2]*INAF – Osservatorio Astrofisico di Arcetri, L.go E. Fermi 5, 50125 Firenze, Italy*
[3]*Harvard–Smithsonian Center for Astrophysics, 60 Garden Street, Cambridge, MA 02138, USA*
[4]*INAF – Osservatorio Astronomico di Roma, via di Frascati 33, 00040 Monte Porzio Catone (RM), Italy*

ABSTRACT

We present a 5–8 μm analysis of the *Spitzer* spectra of 71 ultraluminous infrared galaxies (ULIRGs) with redshift $z < 0.15$, devoted to the study of the role of active galactic nuclei (AGN) and starbursts (SBs) as the power source of the extreme infrared emission. Around ∼5 μm, an AGN is much brighter (by a factor of ≈30) than an SB of equal bolometric luminosity. This allows us to detect the presence of even faint accretion-driven cores inside ULIRGs: signatures of AGN activity are found in ∼70 per cent of our sample (50/71 sources). Through a simple analytical model, we are also able to obtain a *quantitative* estimate of the AGN/SB contribution to the overall energy output of each source. Although the main fraction of ULIRG luminosity is confirmed to arise from star formation events, the AGN contribution is non-negligible (∼23 per cent) and is shown to increase with luminosity. The existence of a rather heterogeneous pattern in the composition and geometrical structure of the dust among ULIRGs is newly supported by the comparison between individual absorption features and continuum extinction.

Key words: galaxies: active – galaxies: starburst – infrared: galaxies.

1 INTRODUCTION

Since a significant population of ultraluminous infrared galaxies (ULIRGs; i.e. the sources whose 8–1000 μm luminosity exceeds $L_{IR} > 10^{12} L_\odot$) was discovered during the *IRAS* all-sky survey (Houck et al. 1985), the origin of their huge infrared (IR) emission has been widely debated. Extreme IR activity is known to be closely related to interacting or merging systems: optical and near-IR imaging shows that a large part of ULIRGs is indeed resulting from the collision of gas-rich galaxies (e.g. Clements et al. 1996; Scoville et al. 2000). Multiwavelength observations have pointed out that the typical spectral energy distribution (SED) of ULIRGs is characterized by a prominent far-IR peak due to dust reprocessing of higher frequency primary radiation, whose elusive source is supposed to be a combination of merger-induced bursts of star formation and gas accretion on to a supermassive black hole. Despite their low frequency and limited contribution to the energy density of the local Universe (Soifer & Neugebauer 1991), nearby ULIRGs represent the counterparts of both the submillimetre sources (Blain et al. 2002

and references therein) and the 24 μm-selected galaxies that are responsible for the dominant energy output at high redshift (Caputi et al. 2007). Understanding their nature and physical properties is therefore a task of great importance, with far-reaching implications for models of structure formation and galaxy evolution. In particular, many efforts have been made in order to assess the contribution of the starburst (SB) and active galactic nucleus (AGN) components to ULIRGs: such an estimate would give deeper insight into the history of star formation over cosmic time and the origin of the X-ray and far-IR backgrounds.

All the diagnostic studies concerning ULIRGs have to come to terms with the great opacity of their nuclear regions that precludes a straight identification of the hidden power source. Nevertheless, the mid-IR thermal emission is expected to suffer from little extinction, and at the same time to preserve some relic signatures of the underlying engine, making this wavelength range very attractive for solid ULIRG diagnostics. With the coming of the *Spitzer Space Telescope* (Werner et al. 2004) and its infrared spectrograph (IRS; Houck et al. 2004), high-quality mid-IR spectra of several tens of local ULIRGs have become available. We have therefore been able to perform a 5–8 μm spectral analysis of a sample of 71 local ULIRGs, separating the AGN and SB components in the observed emission and

★E-mail: nardini@arcetri.astro.it

providing a quantitative estimate of the AGN/SB contribution to the bolometric luminosity of each source.[1] The preliminary results have been anticipated in a recent letter (Nardini et al. 2008, hereafter Paper I), mainly focused on the presentation of the decomposition method. In the present work, we will discuss in detail our findings and investigate their implications. The outline of this paper is as follows: in Section 2, we briefly review the main studies, from radio to X-rays, that have contributed to clarify the multiwavelength picture of ULIRGs. Section 3 illustrates the physical motivations for 5–8 μm diagnostics and describes how recent *Spitzer* observations have prompted our AGN/SB decomposition effort. The ULIRG sample is presented in Section 4, while Section 5 concerns observations and data reduction. In Section 6, we summarize the fitting model and all the analytical steps leading to the estimate of the AGN/SB contribution to the bolometric luminosity. The comparison between our results and those obtained at different wavelengths is provided in Section 7, and the main implications of our findings are discussed in Section 8. The conclusions are drawn up in Section 9, and all the fits are shown in the Appendix along with further considerations on some notable objects.

2 REVIEW OF ULIRG DIAGNOSTICS

The detection of a faint or obscured AGN and the estimate of its contribution to the bolometric luminosity of the hosting galaxy are the main open issues in the study of ULIRGs. This task is complicated because of the dust reprocessing that smoothes the intrinsic differences between the primary AGN and SB radiation fields. A detailed knowledge of the broad-band intrinsic emission of both AGN and SBs is then essential in order to find some signatures of the buried energy source.

In the optical, ULIRGs are classified on the basis of intensity ratios, involving emission lines with different excitation energies to test the hardness of the radiation field. However, dust extinction and reddening affect the use and reliability of such optical diagnostics in various ULIRGs; moreover, the possibility of a differential extinction of the AGN and SB components is difficult to take into account. Qualitatively, compelling evidence of AGN activity is found in a modest fraction of the 118 ULIRGs included in the *IRAS* 1 Jy sample (Kim & Sanders 1998), with a possible trend of increasing AGN detection rate in sources of higher luminosity (Veilleux, Kim & Sanders 1999a). At $L_{IR} > 2 \times 10^{12} L_{\odot}$, nearly a half of IR galaxies exhibit the typical features of Seyfert galaxies, and the fraction of AGN-like objects is even larger if one includes the sources classified as low-ionization nuclear emission-line regions (LINERs). The connection between AGN and LINERs is anyway controversial, because the ionization degree of the latter can be a possible consequence of the supernova-driven shocks and the violent galactic winds pervading an SB as well (Lutz, Veilleux & Genzel 1999; Taniguchi et al. 1999). This leaves the issue about the fraction of ULIRGs actually hosting an AGN unsolved.

The dust opacity affecting the optical, ultraviolet (UV) and near-IR domains turns irrelevant at radio wavelengths, which in principle also benefit of a much higher angular resolution accessible through interferometry. Unfortunately, these advantages are reduced

by the low radio emission of ULIRGs. Nevertheless, although jet-like structures or extended lobes have never been found in ULIRGs, many of them present compact radio cores whose power does not correlate with the Hα luminosity nor with other usual indicators of star formation (Nagar et al. 2003). Better spatial resolution is required to confirm the AGN nature of such sources and rule out any hypothesis of a compact cluster of stars.

Speculatively, the optimal spectral region to clear all the ambiguities and detect the AGN component is the 2–10 keV band, where it is possible to look through the obscuring material and take advantage of the sharp difference between the hard X-ray features and luminosity of SBs and AGN. As a matter of fact, the circumnuclear mixture of gas and dust can be Compton-thick, with equivalent column densities in excess of 10^{24} cm^{-2}, and bury an AGN even in this energy range. Moreover, ULIRGs are faint emitters, since their typical hard X-ray flux is usually far less than $\sim 10^{-3}$ times their IR flux (e.g. Risaliti et al. 2000). Hence, the current instrumentation allows the X-ray diagnostics for a handful of bright sources only: intense star formation activity is confirmed to be the dominant power supply for extreme IR luminosity, and even if convincing traces of elusive AGN (i.e. missed in the optical; Maiolino et al. 2003) are found, the conclusions are still tentative (Franceschini et al. 2003; Ptak et al. 2003).

In the mid- and far-IR, the reprocessed radiation still provides some clues to the enigmatic energy source, that can be recognized, for example, in the circumnuclear dust composition, in the SED large-scale profile and/or in the appearance of coronal lines. An empirical indicator of star formation is usually considered to be the group of emission features centred at 3.3, 6.2, 7.7, 8.6 and 11.3 μm, and attributed to polycyclic aromatic hydrocarbons (PAHs): these features are prominent in dusty environments exposed to soft UV radiation but strongly suppressed in the presence of harder radiation fields, probably because of the alteration/destruction of their carriers (Voit 1992). The concurrent use of PAH strength and appropriate line ratios, for example [O IV]/[Ne II] and [Ne V]/[Ne II], results in an effective probe into the nature of ULIRGs (Genzel et al. 1998). Yet the diagnostic methods based exclusively on emission lines cannot be easily applied to faint sources. This involves the necessity of introducing the continuum properties and mid-IR colours as alternative diagnostic tools, as suggested by Laurent et al. (2000), with the replacement of the line ratio with the ratio between the warm and the hot dust continua. A critical shortcoming actually remains, consisting in the possible non-detection of a weak AGN inside the ULIRG: an unresolved AGN component which is heavily absorbed or intrinsically feeble can vanish within the much more diffuse and intense SB emission.

3 THE AGN/SB SPECTRAL DECOMPOSITION AT 5–8 μM

In order to overcome the potential AGN-dilution effect, it is necessary to select the wavelength range in which the imbalance between the AGN and SB components is maximum. By examining the average SEDs of both AGN and SBs, one immediately evinces that an AGN is much brighter than an SB with equal bolometric luminosity not only in the hard X-ray domain, but also in a narrow IR band stretching from $\sim$3 μm, where the red tail of direct stellar emission begins to vanish, up to $\sim$8 μm, at the onset of the possible silicate absorption feature centred at 9.7 μm (see Fig. 1). This difference can be ascribed to the more intense UV radiation field of the AGN, which is able to heat the dust located in proximity of the central energy source up to the sublimation temperature

---

[1] The bolometric luminosity of a ULIRG is usually dominated by its 8–1000 μm emission: throughout this paper, the terms *bolometric luminosity* and *IR luminosity* are consequently used with an equivalent meaning.
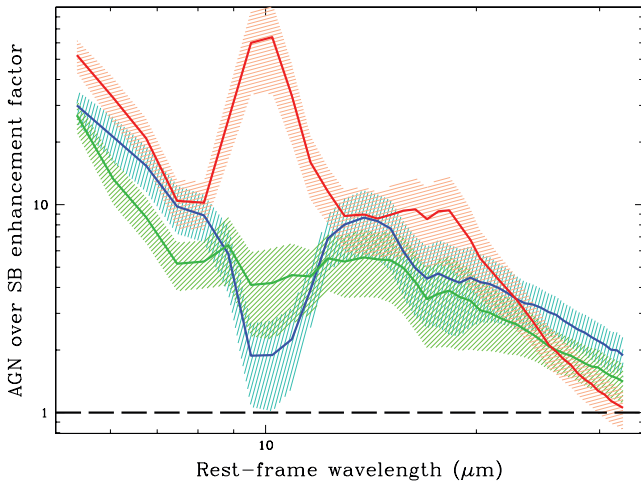
Figure 1. Dependence from wavelength in the *Spitzer*–IRS operative window of the AGN over SB brightness ratio for equal bolometric energy output. The curves are obtained by dividing the observed emission of IRAS 07598+6508 (red line), IRAS 08572+3915 (blue line) and IRAS 12127−1412 (green line) by that of our SB template, whose definition is described in the text. The shaded regions show the 1σ rms uncertainty, and the spectral resolution has been degraded in order to smooth the dependence of the ratios from narrow features. The three objects appear as AGN-dominated at a visual inspection, with moderate reddening, significant absorption and/or suppression of aromatic features. After our analysis, the AGN bolometric contribution to each source turns out to exceed 80 per cent. It is clear how the AGN spectral enhancement rapidly decreases with increasing wavelengths, giving rise to a dilution effect that precludes the detection of intrinsically faint or heavily obscured AGN components. Concerning the red curve, the prominent 10 μm bump and the following plateau are exclusively due to the lack of silicate absorption, which is unusual in composite ULIRGs. Colour figures are available to view online.

($T_{sub} \sim 1500$ K for graphite grains). Incidentally, both the above-mentioned mid-IR *colour* diagnostic and the previous identification of a subset of *warm* ULIRGs (Sanders et al. 1988) are based on a completely similar argument. It is only in the recent years that this spectral region and its potential in the study of ULIRGs have been exploited quantitatively (e.g. Risaliti et al. 2003, 2006a). In particular, *L*-band spectroscopy ($\sim$3–4 μm) has proven to be a powerful method to uncover a buried AGN inside a ULIRG, thanks to diagnostic features like the equivalent width of the 3.3 μm PAH emission and the continuum slope (Risaliti et al. 2006b). Specifically, a steeply rising continuum hints at the reddening of a point-like energy source; an obscured AGN interpretation can also be supported by the simultaneous detection of deep absorption profiles at $\sim$3.4 and $\sim$4.5 μm due to aliphatic hydrocarbons and carbon monoxide, respectively (Sani et al. 2008). Ground-based observations are anyway affected by the strong variability of atmospheric transmission and the high thermal background. For this reason, the quality of the current *L*- and *M*-band spectra, even if obtained with large-aperture facilities like Subaru and Very Large Telescope, allows the determination of the AGN and SB components for only the $\sim$20 brightest ULIRGs. In this view, the spectral capabilities at 2.5–5 μm of the *Akari* satellite look very promising (e.g. Oyabu et al. 2009).

A significant progress has been possible thanks to *Spitzer*, whose spectrograph operates longwards of 5 μm and provides the natural extension of our diagnostic study. The luminosity enhancement of the AGN over the SB component is expected to substantially fade and turn over with increasing wavelength (Fig. 1), none the less at 5–8 μm the considerably higher accuracy achieved from

space still overrides this effect and allows a precise determination of the AGN and SB properties in a composite ULIRG. Before proceeding with the details of our diagnostic technique, it is worth exploring the possibility for a luminous but extremely obscured AGN to be missed even at 5–8 μm. We consider the test case of a source whose IR luminosity arises in equal parts from nuclear activity and star formation. A contribution of 20 per cent to the observed 5–8 μm emission can be assumed as a reasonable detection limit for the AGN component, which intrinsically is expected to outshine the SB counterpart by a factor of $\sim$20–30 in this spectral range. Consequently, the AGN should undergo a flux attenuation of approximately two orders of magnitude in order to fall below the detection threshold. In terms of a standard extinction law, this corresponds to a screen extinction of $A_V \sim 200$ mag ($A_{6\,\mu m}/A_V \sim 0.025$; Nishiyama et al. 2008, 2009). This scenario is possible but unlikely (see also Section 6 and the discussion in Genzel et al. 1998). We are then confident that virtually all the luminous AGN components inside ULIRGs can be probed through 5–8 μm *Spitzer*–IRS spectra.

The unprecedented sensitivity of the mid-IR capabilities onboard *Spitzer*, in fact, has made it possible to reconstruct with high precision the SEDs of large samples of luminous active nuclei and SB galaxies, and a surprising spectral homogeneity has been found within the two separate classes. At the highest luminosities, this is especially true in the 5–8 μm range, with nearly constant shapes of both the aromatic complex in SBs (Brandl et al. 2006, hereafter B06) and the continuum in AGN (Netzer et al. 2007, hereafter N07). Larger differences come out at longer wavelengths, where the temperature and emissivity of the different dust components as well as radiative transfer need to be taken into account. Our strategy then aims at disentangling the AGN and SB contributions to the observed 5–8 μm emission of ULIRGs by means of spectral templates, whose success hinges upon the large difference between the average AGN/SB emission and the small dispersion within the AGN and SB spectral classes. In the following, we explain in detail the physical reasons which justify the selection of the AGN and SB templates for this work.

Starburst. As previously mentioned, the mid-IR spectra of SB galaxies display little variations from one object to another, especially in the 5–8 μm wavelength range. At first sight this appears to be a singular circumstance, because of the large number of physical variables involved in determining the observed properties of an SB: these include the initial mass function, the duration and evolutionary stage of the single bursts, the properties of the dust grains and those of the interstellar environment, and obviously the total mass and luminosity of the system. It has already been suggested in B06 that such a remarkable similarity can derive from the spatial integration over a huge number of unresolved star-forming spots: this is indeed an interesting point that should be investigated further. The typical SB emission in the 5–8 μm interval is characterized by two prominent aromatic features centred at 6.2 and 7.7 μm. In SB-dominated ULIRGs, the shape of these lines and their intensity ratio slightly differ from those observed in lower luminosity SBs (like NGC 7714), probably because of higher obscuration in the former (Rigopoulou et al. 1999). Moreover, the reliability of PAHs as quantitative tracers of star formation is still debated (Förster Schreiber et al. 2004; Peeters, Spoon & Tielens 2004). In order to properly describe the SB component in our spectra, and check if the prescription of little dispersion may be applied in the ULIRG luminosity range as well, we performed a preliminary analysis on a representative subset of sources that other multiband diagnostics have established to host powerful SBs. The 5–8 μm emission of
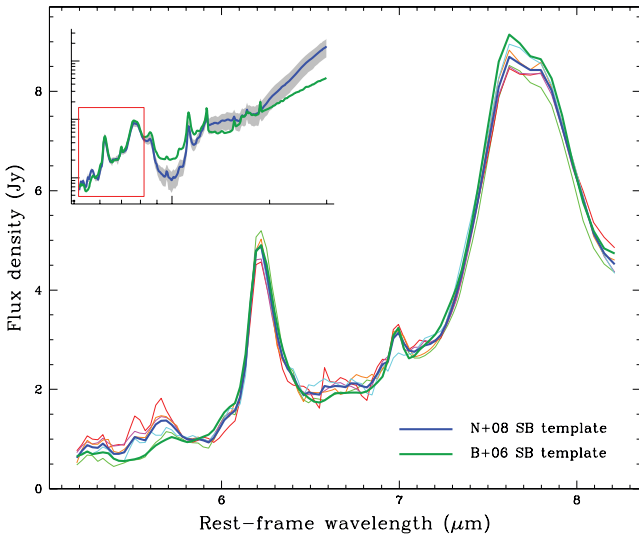
Figure 2. Comparison between our SB template (blue solid line) and that of B06 (deep green dashed line) at 5–8 μm. Their behaviour up to ~30 μm is outlined in a log–log scale in the top-left corner. The single spectra of the five sources employed in our template have also been plotted with lines of different colour: IRAS 10190+1322 (light green), IRAS 12112+0305 (red), IRAS 17208−0014 (magenta), IRAS 20414−1651 (orange) and IRAS 22491−1808 (cyan).

these sources has been approximated by means of two Gaussian profiles for the aromatic features and a power-law continuum.[2] As a result, the main properties of the PAH features turn out to be the same observed in lower luminosity systems. Their equivalent width is confirmed not to depend on the global IR output, and the modest spread concerning their relative strength has already been related to internal obscuration; the slope of the underlying continuum is $\Gamma_{SB} \gtrsim 4$, roughly uniform and well above the value assumed for the AGN component (see later). This tight correlation between the properties of the PAH features and the dust continuum is brought out also in B06, hence we are justified in the use of a spectral template to represent through a single scale factor the SB component of ULIRGs. A complete characterization of the whole SB spectrum would of course require a detailed model involving many parameters, and this indeed remains unavoidable when considering larger spectral domains.

Instead of adopting a prototypal SB template from the literature, we have constructed a new one as the average spectrum of the five brightest SB-dominated sources in our sample, i.e. IRAS 10190+1322, IRAS 12112+0305, IRAS 17208−0014, IRAS 20414−1651 and IRAS 22491−1808. The resulting slope is $\Gamma_{SB} \simeq$ 4.2, and the equivalent widths of the aromatic features are 0.43 and 0.88 μm: such values do not actually differ from the measures of B06, as can be easily evinced from Fig. 2. The comparison between our SB template and that of B06 over the entire IRS spectral range has already been shown in Paper I, in order to emphasize their divergence just longwards of ~8 μm. This is anyway displayed again in the box of Fig. 2, where we focus instead on their similarity over the wavelengths of interest. Such similarity (and the fact that the

PAH equivalent widths are the largest among ULIRGs) rules out any possibility of significant AGN contamination in our SB template.[3]

Summarizing, the spectral slope of the observed 5–8 μm ULIRG continuum is very sensitive to the possible AGN contribution. The PAH features and their intensities play of course an important role in modelling the spectral shape, but the dispersion in their properties which is found in pure SBs is actually too small to alter the determination of the continuum, mimicking the presence of a bolometrically significant AGN in a composite source.

Active galactic nucleus. At the wavelengths of concern, the AGN emission is dominated by the cooling of small dust grains that are transiently heated up to temperatures close to the sublimation limit. Such a process is expected to produce a nearly featureless power-law continuum, and yet aromatic features are found in several quasars, as confirmed by recent observations (Schweitzer et al. 2006; Lutz et al. 2007, 2008). The inferred star formation rate can be very high, and raises the question on the extent of the stellar contamination in the observed spectra of quasars and the reliability of a pure AGN template. In N07, the far-IR emission of a large set of Palomar-Green (PG) quasars is ascribed to cold dust in extended regions, and then suspected of having a stellar origin; the contribution of star formation to be subtracted in order to determine the intrinsic SED of a type 1 AGN is obtained from the properties of 12 SB-dominated ULIRGs. The resulting average spectrum can be modelled by a single power law from ~3 μm to the 9.7 μm silicate bump (which usually appears in emission whenever the source is not obscured). The most striking outcome is that the spectral dispersion at these wavelengths is very small if compared to the large differences found in the far-IR. It is then reasonable to adopt a power-law component to reproduce the 5–8 μm AGN flux density. The choice of the spectral index however is not immediate, and has to be briefly discussed. A coarse estimate, as deduced from the SEDs provided by N07, yields $\Gamma_{AGN} \sim 0.7$; a better value can be anyway achieved from our *L*-band study. The reason is that we are dealing with an active nucleus component in a ULIRG environment, and the overall dust properties are expected to differ from those of the PG quasars in the N07 sample. In Fig. 3, we show the spectral template obtained by averaging the *L*-band emission of four ULIRGs in our sample known to host a fairly unobscured active nucleus: MRK 231, IRAS 15462+0450 and IRAS 21219−1757, which are optically classified as type 1 Seyfert galaxies, and IRAS 05189−2524, which is a type 2. For all these sources, the *L*-band emission consists of a strong continuum arising from the dust heated by the AGN, as also confirmed by the small equivalent width of the 3.3 μm aromatic feature, only reaching a few nm while usually exceeding ~100 nm in pure SBs (Moorwood 1986; Imanishi & Dudley 2000). The mean value of the continuum slope is ~1.5, and such a value has then been assumed for the present analysis. Its extrapolation to 5–8 μm is supported by N07, since no significant change in the continuum gradient is expected. Moreover, the same 5–8 μm spectra of the four template sources are fully consistent with the stretching of their *L*-band slope, in spite of the growing aromatic emission. The slight discrepancy between these estimates of the AGN spectral index, based on different samples, seems to be a natural consequence of the greater obscuration characterizing the ULIRG environment, rather than of a significant stellar contamination even at such short wavelengths. As mentioned, the unobscured AGN components of

---

[2] Throughout this paper, we describe the emission in terms of the flux density $f_\nu(\lambda)$, hence all the spectral indices of the power-law components in the following are defined as $f_\nu(\lambda) \propto \lambda^\Gamma$.

[3] We also note that in this case our AGN/SB spectral decomposition would have brought out the necessity of a *negative* AGN contribution in order to optimally fit the shape of a genuine SB-dominated ULIRG.
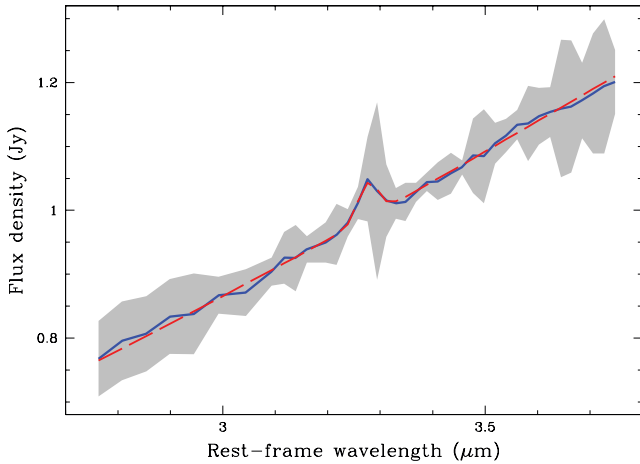
Figure 3. The blue solid line represents the average *L*-band spectrum of a source whose near-IR emission is dominated by an unobscured AGN; the shaded area encompasses the 1σ rms dispersion. The best fit (red dashed curve) requires two components: a power law with spectral index 1.51 ± 0.09 and a Gaussian line with equivalent width <3 nm, far below the typical values of the PAH emission in SB galaxies ($\sim$100 nm).

this work and the PG quasars of N07 (even though intense star formation is in place) are different populations, in terms of both the luminosity of the AGN and the properties of the absorbing medium. A higher covering factor of the dust surrounding the AGN component in a ULIRG environment can account for a steeper intrinsic slope. The covering factor is indeed shown to decrease as a function of the AGN luminosity (Maiolino et al. 2007).

Beyond these aspects, another crucial effect has to be considered: the active nucleus component is still extremely compact, and the AGN-related hot dust emission can be extinguished by an external screen, consisting either of the outer layers of the obscuring torus predicted in unification models (Antonucci 1993) or of a thick absorbing cloud along the line of sight. We have therefore introduced a wavelength-dependent attenuation factor $e^{-\tau(\lambda)}$, assuming for the optical depth a power-law behaviour $\tau(\lambda) \propto \lambda^{-1.75}$ (Draine 1989). On the contrary, the SB component can easily extend over several hundreds of pc, and therefore can be affected exclusively by internal extinction, which is already embodied in the shape of the template: in fact, even if the SB extinction becomes apparent when considering the silicate absorption profiles at longer wavelengths, the 5–8 μm emission does not seem to be significantly modified except for the limited dispersion in the PAH ratio.

In Section 8, we will deal again (from a quantitative point of view) with the intrinsic slope of the AGN continuum emission, investigating its interplay with the shape of the extinction law, and how any change can affect the AGN/SB spectral decomposition and the subsequent estimate of the relative AGN/SB bolometric contribution.

4 THE ULIRG SAMPLE

The present sample consists of 71 objects and is fully representative of the ULIRG population in the local Universe. In order to avoid a bias towards AGN activity, the flux limitation has been adopted at 60 μm. The 60 μm flux density is in fact a good proxy of the cold dust component, and this translates into a fairly unbiased selection with respect to the nature of the energy source. All the ULIRGs in the already mentioned 1 Jy sample with available *Spitzer*–IRS observations and the additional requirement of a redshift $z < 0.15$

have been selected, for a total of 63 objects. With respect to Paper I, three extra sources have been added, i.e. IRAS 02021−2103, IRAS 07598+6508 and IRAS 08559+1053. The broad absorption line Seyfert 1 galaxy IRAS 07598+6508, that was initially dropped since a significant fraction of its mid-IR emission was expected to have a non-thermal origin, and IRAS 08559+1053, that was only observed during the in-flight calibration phase of *Spitzer* (by J. R. Houck), have been retrieved for completeness. We point out that the volume restriction is absolutely arbitrary in this context, since it is directly imported from our previous studies, being it necessary to apply our *L*-band diagnostics. The 1 Jy sample indeed contains 70 objects meeting this selection requirement. No observation is anyway available for the seven missing sources: only four has been recently observed with *Spitzer*, but archive data are not provided as yet; the other three have not been observed. Within this uncovered subset, five objects are optically classified as Seyfert 2 galaxies, while two are unclassified. The consequent bias is then minor, and will be discussed later on when we assess the incidence of black hole accretion and star formation at extreme IR luminosities.

Summarizing, all the selected targets obey the following criteria: (1) a redshift $z < 0.15$ and (2) a 60 μm *IRAS* flux density $f_{60} > 1$ Jy. The statistics are already large enough to derive general conclusions about the local ULIRG population. However, being the 1 Jy sample also characterized by constraints on the position of the target, a systematic search for ULIRGs inside the *IRAS* 2 or 1.2 Jy all-sky samples (Strauss et al. 1992; Fisher et al. 1995, respectively) would yield a wealth of additional sources fulfilling the present criteria. We decided to complete our sample by adding only the eight sources drawn from the 2 Jy sample which are already present in Genzel et al. (1998), since they are among the brightest and best-studied ULIRGs.

The main properties of all the sources in our sample are listed in Table 1. NGC 6240 is the only source that does not strictly comply with the ULIRG classification, because of its slightly lower IR luminosity. It is anyway an advanced merger showing all the morphological and physical properties of ULIRGs, and is usually included in this class. Concerning this, it is also important to specify that the total IR luminosity of our sources has been computed according to the broad-band flux equation in Sanders & Mirabel (1996):

$$F_{IR} = 1.8 \times 10^{-11}(13.48 f_{12} + 5.16 f_{25} + 2.58 f_{60} + f_{100}), \quad (1)$$

where F_{IR} is the total IR flux in units of erg s^{-1} cm^{-2} and f_{12}, f_{25}, f_{60} and f_{100} are the *IRAS* flux densities in Jy. When only an upper limit is available for f_{12} (and f_{25}), we have simply assumed the one-half of this limit. Such strategy provides a good approximation of the true flux density if compared to the few estimates proposed in Kim & Sanders (1998). The luminosity distances have been obtained making use of a standard cosmology with $H_0 = 70$ km s^{-1} Mpc^{-1}, $\Omega_m = 0.27$ and $\Omega_\Lambda = 0.73$ (Hinshaw et al. 2009).

5 OBSERVATIONS AND DATA REDUCTION

The spectroscopic observations of all the sources in our sample were obtained with the *Spitzer*–IRS low-resolution modules, within three different programmes devoted to buried activity in ULIRGs and massive mergers:[4] the programme IDs are 105, 2306 and 3187, and the principal investigators are J. R. Houck, M. Imanishi and S. Veilleux, respectively. The details concerning each observation are

---

[4] The only exception is IRAS 08559+1053, as mentioned.

Table 1. General properties of the 71 sources in our sample.

Object	z	D_L	f_{12}	f_{25}	f_{60}	f_{100}	$\log(L_{IR}/L_\odot)$	Class
ARP 220	0.018	79	0.61:	8.00:	104.09:	115.29:	12.18	IIIb
IRAS 00091−0738	0.118	554	<0.07	0.22	2.63	2.52	12.27	IIIb
IRAS 00188−0856	0.128	604	<0.12	0.37	2.59	3.40	12.42	V
IRAS 00456−2904	0.110	513	<0.08	0.14	2.60	3.38	12.23	IIIa
IRAS 00482−2721	0.129	608	<0.10	<0.18	1.13	1.84	12.09	IIIb
IRAS 01003−2238	0.118	550	<0.23	0.66	2.29	1.79	12.33	V
IRAS 01166−0844	0.118	553	<0.14	0.17	1.74	1.42	12.13	IIIb
IRAS 01298−0744	0.136	644	<0.12	<0.28	2.47	2.08	12.37	IVb
IRAS 01569−2939	0.141	669	<0.11	0.14	1.73	1.51	12.27	IVa
IRAS 02021−2103	0.116	541	<0.07	0.30	1.45	1.72	12.09	IVa
IRAS 02411+0353	0.144	683	<0.08	0.22	1.37	1.95	12.28	IIIb
IRAS 03250+1606	0.129	607	<0.10	<0.15	1038	1.77	12.12	IVb
IRAS 04103−2838	0.117	549	0.08	0.54	1.82	1.71	12.24	IVb
IRAS 05189−2524	0.043	189	0.74:	3.47:	13.25:	11.84:	12.17	IVb
IRAS 07598+6508	0.148	707	0.26	0.53	1.69	1.73	12.54	IVb
IRAS 08559+1053	0.148	706	<0.10	0.19	1.12	1.95	12.26	IVb
IRAS 08572+3915	0.058	261	0.33:	1.76:	7.30:	4.77:	12.16	IIIb
IRAS 09039+0503	0.125	587	<0.17	<0.21	1.48	2.06	12.17	IVa
IRAS 09116+0334	0.145	691	<0.09	<0.14	1.09	1.82	12.18	IIIa
IRAS 09539+0857	0.129	607	<0.15	<0.15	1.44	1.04	12.11	V
IRAS 10190+1322	0.077	348	<0.10	0.38	3.33	5.57	12.06	IIIb
IRAS 10378+1109	0.136	645	<0.11	0.24	2.28	1.82	12.36	IVb
IRAS 10485−1447	0.133	628	<0.11	<0.30	1.73	1.66	12.23	IIIa
IRAS 10494+4424	0.092	423	<0.12	0.16	3.53	5.41	12.21	IVb
IRAS 11095−0238	0.107	495	<0.14	0.42	3.25	2.53	12.28	IVb
IRAS 11130−2659	0.136	644	<0.09	0.20	1.21	1.24	12.14	IVa
IRAS 11387+4116	0.149	709	<0.20	<0.14	1.02	1.51	12.22	V
IRAS 11506+1331	0.127	599	<0.10	<0.29	2.58	3.32	12.36	IVb
IRAS 12072−0444	0.128	604	<0.12	0.54	2.46	2.47	12.41	IVb
IRAS 12112+0305	0.073	332	<0.11:	0.66:	8.18:	9.46:	12.33	IIIb
IRAS 12127−1412	0.133	628	<0.13	0.24	1.54	1.13	12.20	IIIa
IRAS 12359−0725	0.138	654	<0.19	<0.22	1.32	1.12	12.19	IIIa
IRAS 13335−2612	0.125	587	<0.13	<0.14	1.40	2.10	12.13	IIIb
IRAS 13454−2956	0.129	607	<0.06	<0.16	2.16	3.38	12.31	IIIa
IRAS 13509+0442	0.136	643	0.10	<0.23	1.56	2.23	12.30	IVb
IRAS 13539+2920	0.108	504	<0.09	0.12	1.83	2.73	12.09	IIIb
IRAS 14060+2919	0.117	545	<0.10	0.14	1.61	2.42	12.13	IVa
IRAS 14197+0813	0.131	618	<0.17	<0.19	1.10	1.66	12.12	V
IRAS 14252−1550	0.150	714	<0.09	<0.23	1.15	1.86	12.24	IIIb
IRAS 14348−1447	0.083	377	<0.10:	0.55:	6.82:	7.31:	12.36	IIIb
IRAS 15130−1958	0.109	508	<0.14	0.39	1.92	2.30	12.17	IVb
IRAS 15206+3342	0.124	584	0.08	0.35	1.77	1.89	12.25	IVb
IRAS 15225+2350	0.139	659	<0.07	0.18	1.30	1.48	12.18	IVa
IRAS 15250+3609	0.055	247	0.16:	1.31:	7.10:	5.93:	12.06	(IIIb)
IRAS 15462−0450	0.100	461	<0.13	0.45	2.92	3.00	12.22	IVb
IRAS 16090−0139	0.134	631	0.09	0.26	3.61	4.87	12.57	IVa
IRAS 16156+0146	0.132	623	<0.10	0.28	1.13	1.00	12.12	IIIb
IRAS 16468+5200	0.150	716	<0.06	0.10	1.01	1.04	12.12	IIIb
IRAS 16474+3430	0.111	519	<0.13	0.20	2.27	2.88	12.21	IIIb
IRAS 16487+5447	0.104	480	<0.07	0.20	2.88	3.07	12.19	IIIb
IRAS 17028+5817	0.106	492	<0.06	0.10	2.43	3.91	12.18	IIIa
IRAS 17044+6720	0.135	638	<0.07	0.36	1.28	0.98	12.18	IVb
IRAS 17179+5444	0.147	700	<0.08	0.20	1.36	1.91	12.28	IVb
IRAS 17208−0014	0.043	190	0.20:	1.61:	32.13:	36.08:	12.42	(V)
IRAS 19254−7245	0.062	277	0.22	1.24	5.16:	5.79	12.09	(IIIb)
IRAS 20100−4156	0.130	610	<0.13	0.34	5.19:	5.16	12.65	(IIIb)
IRAS 20414−1651	0.087	398	<0.65	0.35	4.36	5.25	12.31	IVb
IRAS 20551−4250	0.043	190	0.28:	1.87:	12.19:	10.31:	12.05	(V)
IRAS 21208−0519	0.130	613	<0.09	<0.15	1.17	1.66	12.08	IIIa
IRAS 21219−1757	0.112	521	0.21	0.45	1.07	1.18	12.14	V
IRAS 21329−2346	0.125	587	<0.08	<0.16	1.65	2.22	12.16	IVa
IRAS 22206−2715	0.131	620	<0.10	<0.16	1.75	2.33	12.23	IIIb

Table 1 – *continued*

Object	z	$D_{\rm L}$	f_{12}	f_{25}	f_{60}	f_{100}	$\log(L_{\rm IR}/{\rm L_\odot})$	Class
IRAS 22491−1808	0.078	353	<0.09	0.55	5.44	4.45	12.20	IIIb
IRAS 23128−5919	0.045	198	0.35:	1.64:	10.94:	10.68:	12.06	(IIIb)
IRAS 23234+0946	0.128	602	<0.06	<0.20	1.56	2.11	12.16	IIIb
IRAS 23327+2913	0.107	496	<0.06	0.22	2.10	2.81	12.13	IIIa
MRK 231	0.042	187	1.83:	8.84:	30.80:	29.74:	12.55	IVb
MRK 273	0.038	167	0.24:	2.36:	22.51:	22.53:	12.18	IVb
NGC 6240	0.024	107	0.59:	3.55:	22.94:	26.49:	11.86	(IIIb)
4C +12.50	0.122	570	<0.14	0.67	1.92	2.06	12.32	IIIb
UGC 5101	0.039	174	0.25:	1.02:	11.68:	19.91:	12.00	(V)

Note. z, $D_{\rm L}$: redshift and luminosity distance (in Mpc). f_{12}, f_{25}, f_{60}, f_{100}: IRAS flux densities (in Jy, with the colon indicating the revisions in Sanders et al. 2003). $L_{\rm IR}$: total IR luminosity computed according to Sanders & Mirabel (1996). Class: morphological classification as defined in Veilleux, Kim & Sanders (2002). IIIa: wide binary (apparent separation >10 kpc); IIIb: close binary (apparent separation <10 kpc); IVa: Diffuse merger; IVb: compact merger; V: old merger. The entries within brackets are derived from Duc, Mirabel & Maza (1997) and Scoville et al. (2000).

listed in Table 2. The local ULIRGs of our sample are *bright* objects, and their signal can be easily distinguished from the background emission, mostly due to zodiacal light. After having verified that a refined reduction of the data was not necessary for our purposes, we decided to perform our analysis beginning from the coadded images provided by the *Spitzer Science Center*. A coadded image is obtained as the average over multiple telescope pointings. At this stage, the individual snapshots have been already processed with the default pipeline (versions 13.0 and upgrades) that among other basic operations includes the linearization and the fitting of the signal ramp, the dark subtraction and the flat-fielding. Since each observation in staring mode consists of two exposures with different positions of the source along the slit, we have subtracted the background emission by taking the difference between the couple of images in the nodding cycle. The spectra have been extracted following the standard steps for point-like sources within the software SPICE. The flux uncertainties have been computed considering the typical Poissonian distribution for source and background counts. The latter are estimated from the companion coadded images, since the off-source subslit provides the background of the nodded on-source observation.

While the wavelength calibration is not a crucial issue in this work, a precise flux calibration is required to derive a reliable estimate of the relative AGN/SB contribution to the bolometric luminosity (see Section 6). In the older versions of the processing pipeline, the accuracy of the absolute flux calibration for the *Spitzer*–IRS low-resolution orders was quoted to be about 20 per cent. Even with such a coarse evaluation, our final results are not substantially modified, hence the *Spitzer* calibration has been adopted. We have anyway checked its reliability against the photometric data provided by *IRAS*. For 53 sources (corresponding to 75 per cent of our sample), the 12 μm *IRAS* flux density is only an upper limit, which is always higher than the *Spitzer*–IRS equivalent. For 16 sources not even the *IRAS* flux at 25 μm is available, while in all the remaining cases the *Spitzer* measure turns out to be fully consistent with the *IRAS* one (it is indeed slightly lower on average, by ∼20 per cent at most). Even if the analysis is restricted to a narrow spectral range and only the short-low (SL) orders are involved, we performed the extraction of the long-low (LL) orders as well, so that we have the entire ∼5–35 μm spectra of more than 60 sources. Only in a few cases, a slight rescaling is necessary for a smooth connection between SL1 and LL2 orders, and this cannot introduce any systematic effect on the measured 25 μm flux. Aperture losses at long

wavelengths can indeed occur when comparing the narrow-slit IRS spectroscopy to the large-aperture *IRAS* photometry. Whatever the right explanation may be, we conclude that the *Spitzer*–IRS calibration at 5–8 μm is fully reliable, and that the normalization of our spectra to match the *IRAS* fluxes, however not possible for the whole sample, is not even required.

6 AGN/SB BOLOMETRIC CONTRIBUTION

The use of spectral templates to model the intrinsic AGN and SB components significantly reduces the number of degrees of freedom in our analytical description. The decomposition method has already been introduced and discussed in detail in Paper I, nevertheless it is useful to examine again the main steps. By defining the 6 μm normalized AGN and SB templates $u_\nu^{\rm AGN}$ and $u_\nu^{\rm SB}$, the observed 5–8 μm ULIRG emission can be parametrized as follows:

$$f_\nu^{\rm obs}(\lambda) = f_6^{\rm int}\left[(1-\alpha_6)u_\nu^{\rm SB} + \alpha_6 u_\nu^{\rm AGN}{\rm e}^{-\tau(\lambda)}\right], \qquad (2)$$

where α_6 is the AGN contribution to the intrinsic (de-absorbed) flux density $f_6^{\rm int}$. Along with the optical depth to the active nucleus $\tau_6 = \tau(6\,\mu{\rm m})$ and apart from the flux normalization, α_6 is the only degree of freedom in our model. The best fits have been found via the minimization of the χ^2. In spite of the large differences observed in our ULIRG spectra, this simple model always provides a good match to the data. Although the best fits usually have a reduced $\chi^2 \gtrsim 2$ and are not formally acceptable in a statistical sense (due to the use of templates that ignores minor features, and the small *Spitzer*–IRS error bars), both the aromatic emission and the continuum shape are well reproduced, with residuals smaller than 10 per cent at all wavelengths.

The fitting procedure allows the determination of $f_6^{\rm int}$ as well, hence we can compute the ratio between the absorption-corrected 6 μm luminosity and the bolometric luminosity of each source, defined as

$$R = \left(\frac{\nu_6 f_6^{\rm int}}{F_{\rm IR}}\right), \qquad (3)$$

where $F_{\rm IR}$ is the total IR flux introduced in equation (1). Since the equivalent quantities for pure AGN and pure SBs (hereafter indicated, respectively, as $R^{\rm AGN}$ and $R^{\rm SB}$) are widely different from each other, R is itself an indicator of the significance of AGN activity within composite sources, and can be used both to test the consistency of our decomposition method and to assess the relative

Table 2. Observation log of our ULIRG sample. All the sources except one have been observed within the following programmes: Spectroscopic study of distant ULIRGs II (PID 105, PI J.R.Houck), Buried AGN in ULIRGs (PID 2306, PI M.Imanishi), The evolution of activity in massive gas-rich mergers (PID 3187, PI S.Veilleux).

Object	PID	Date (UT)	T_{SL}	Object	PID	Date (UT)	T_{SL}
ARP 220	105	2004 February 29	3×14	IRAS 14060+2919	2306	2004 July 16	2×60
IRAS 00091−0738	3187	2005 June 30	2×60	IRAS 14197+0813	3187	2005 February 13	2×60
IRAS 00188−0856	105	2003 December 17	2×60	IRAS 14252−1550	2306	2004 July 17	2×60
IRAS 00456−2904	3187	2005 July 14	2×60	IRAS 14348−1447	105	2004 February 07	1×60
IRAS 00482−2721	3187	2005 July 07	2×60	IRAS 15130−1958	3187	2005 March 15	2×60
IRAS 01003−2238	105	2004 January 04	1×60	IRAS 15206+3342	105	2004 June 24	1×60
IRAS 01166−0844^a	3187	2005 January 03	2×60	IRAS 15225+2350	2306	2005 February 07	2×60
IRAS 01298−0744	105	2005 July 14	2×60	IRAS 15250+3609	105	2004 March 04	3×14
IRAS 01569−2939	2306	2004 July 18	2×60	IRAS 15462−0450	105	2004 March 02	1×60
IRAS 02021−2103	3187	2005 January 15	2×60	IRAS 16090−0139	105	2005 August 05	1×60
IRAS 02411+0353	2306	2005 January 14	2×60	IRAS 16156+0146	3187	2005 March 15	2×60
IRAS 03250+1606	3187	2005 February 11	2×60	IRAS 16468+5200^c	2306	2004 July 14	4×60
IRAS 04103−2838	3187	2005 February 10	2×60	IRAS 16474+3430	2306	2004 July 14	2×60
IRAS 05189−2524	105	2004 March 22	3×14	IRAS 16487+5447	2306	2004 July 17	2×60
IRAS 07598+6508	105	2004 February 29	3×14	IRAS 17028+5817	2306	2004 July 17	2×60
IRAS 08559+1053^b	666	2003 November 23	2×60	IRAS 17044+6720	2306	2004 July 17	2×60
IRAS 08572+3915	105	2004 April 15	3×14	IRAS 17179+5444	105	2004 April 17	2×60
IRAS 09039+0503	3187	2005 April 18	2×60	IRAS 17208−0014	105	2004 March 27	3×14
IRAS 09116+0334	2306	2005 April 21	2×60	IRAS 19254−7245	105	2005 May 30	3×14
IRAS 09539+0857	3187	2005 June 05	2×60	IRAS 20100−4156	105	2004 April 13	1×60
IRAS 10190+1322^c	3187	2005 May 22	4×60	IRAS 20414−1651	105	2004 May 14	1×60
IRAS 10378+1109	105	2005 June 08	2×60	IRAS 20551−4250	105	2004 May 14	2×14
IRAS 10485−1447	3187	2005 May 23	2×60	IRAS 21208−0519^d	3187	2004 November 13	2×60
IRAS 10494+4424	2306	2004 November 17	2×60	IRAS 21219−1757	3187	2004 November 16	2×60
IRAS 11095−0238	105	2005 June 07	2×60	IRAS 21329−2346	3187	2004 November 16	2×60
IRAS 11130−2659	2306	2005 July 12	2×60	IRAS 22206−2715	3187	2004 November 15	2×60
IRAS 11387+4116	2306	2005 January 11	2×60	IRAS 22491−1808	105	2004 June 24	1×60
IRAS 11506+1331	3187	2005 May 25	2×60	IRAS 23128−5919	105	2004 May 11	3×14
IRAS 12072−0444	105	2004 January 06	1×60	IRAS 23234+0946	3187	2004 December 13	2×60
IRAS 12112+0305	105	2004 January 04	3×14	IRAS 23327+2913	2306	2004 December 08	2×60
IRAS 12127−1412	3187	2005 June 30	2×60	MRK 231	105	2004 April 14	2×14
IRAS 12359−0725	2306	2005 June 30	2×60	MRK 273	105	2004 April 14	2×14
IRAS 13335−2612	3187	2005 February 15	2×60	NGC 6240	105	2004 March 04	2×14
IRAS 13454−2956^c	3187	2005 July 14	4×60	4C+12.50	105	2004 January 07	3×14
IRAS 13509+0442	2306	2004 July 17	2×60	UGC 5101	105	2004 March 23	3×14
IRAS 13539+2920	2306	2005 February 07	2×60				

Note. T_{SL}: integration time in number of cycles times seconds for the IRS SL orders (SL2: ∼5.2–7.7 μm; SL1: ∼7.4–14.5 μm). Since each cycle consists of two nod positions, the total observing time per slit is obtained by multiplying these entries by an additional factor of 2. ^{a}Southern nucleus. The northern one is also observed but is much fainter. ^{b}Observation performed during the in-orbit checkout phase (IRS campaign P: PID 666, PI J.R.Houck). ^{c}Both nuclei are observed but apparently not completely resolved. ^{d}Northern nucleus. The southern one is also observed but is much fainter.

AGN/SB contribution in terms of bolometric luminosity. By rendering explicit the AGN and SB components within equation (3), respectively, as $\alpha_6 f_6^{int}$ and $(1 - \alpha_6) f_6^{int}$, and decomposing F_{IR} as $F_{IR}^{AGN} + F_{IR}^{SB}$, the dependence of R on α_6, R^{AGN} and R^{SB} can be brought out through a simple algebra:

$$R = \frac{R^{AGN} R^{SB}}{\alpha_6 R^{SB} + (1 - \alpha_6) R^{AGN}}. \tag{4}$$

This theoretical R–α_6 relation has been fitted to our data, with R^{AGN} and R^{SB} as floating variables. In Paper I, we obtained that $R^{AGN}/R^{SB} \sim 28$; we have anyway decided to repeat the evaluation of these critical parameters, because some fits have been improved with respect to the previous work and three extra sources have been added to the sample. The new results are in good agreement with the previous ones:

$$\log R^{AGN} = -0.55^{+0.06}_{-0.07} \quad \text{and} \quad \log R^{SB} = -1.91^{+0.02}_{-0.02}.$$

Taking $R^{AGN}/R^{SB} \sim 23$, we are able to provide a quantitative estimate of the AGN contribution ($\alpha_{bol} = F_{IR}^{AGN}/F_{IR}$) to the bolometric luminosity of each source, as

$$\alpha_{bol} = \frac{\alpha_6}{\alpha_6 + (R^{AGN}/R^{SB})(1 - \alpha_6)}. \tag{5}$$

The values of α_{bol} are listed in Table 3. Incidentally, it should be noted that a value $\alpha_{bol} \approx 1$ is not reached even in optically bright quasars, since the contamination from star formation activity is always present and non-negligible. In Fig. 4(a), we show the relation between R and α_{bol}, which can be expressed in the neat and manifest form $R = \alpha_{bol} R^{AGN} + (1 - \alpha_{bol}) R^{SB}$ by inverting equation (5).

The regularity of the pattern shaped by the location of the sources in this plot is in itself a qualitative validation of our method. We have anyway performed a further test of self-consistency, by computing

Table 3. Spectral parameters and AGN contribution for the 71 ULIRGs in our sample. All the optical depths refer to the AGN component: a colon indicates the upper limits evaluated from the residuals to the best fit. α_6: AGN contribution to the intrinsic (i.e. de-absorbed) continuum emission at 6 μm (in per cent). τ_6: optical depth to the AGN continuum at 6 μm according to the power-law prescription for reddening. $\alpha_{\rm bol}$: AGN contribution to the bolometric luminosity (in per cent). These entries are only affected by the statistical uncertainty both in the flux amplitude of the AGN/SB components and in the average ratios $R^{\rm AGN}$ and $R^{\rm SB}$. The systematic effects are discussed and quantified in the text. $\tau_{\rm ice}$: optical depth of the ∼6.0 μm absorption feature due to water ice. $\tau_{\rm HAC,1}$, $\tau_{\rm HAC,2}$: optical depths of the companion features attributed to hydrogenated amorphous carbons (HAC), centred at ∼6.85 and ∼7.25 μm, respectively. α_6^*, τ_6^*, $\alpha_{\rm bol}^*$: same as α_6, τ_6 and $\alpha_{\rm bol}$, obtained by assuming a spectral slope of 0.7 (instead of 1.5) for the AGN template (see Section 8). $V/L/X$: spectral classification in the visible, L band and hard X-rays. ⋆: starburst; ⊗: LINER; ●: AGN detection; ⊙: AGN detection, tentative.

Source	α_6	τ_6	$\alpha_{\rm bol}$	$\tau_{\rm ice}$	$\tau_{\rm HAC,1}$	$\tau_{\rm HAC,2}$	α_6^*	τ_6^*	$\alpha_{\rm bol}^*$	$V/L/X$
ARP 220	84 ± 1	1.47 ± 0.01	18^{+4}_{-3}	<2.13	0.29 ± 0.01	$<0.21:$	90 ± 1	2.00 ± 0.01	20^{+4}_{-3}	$\otimes^1 \star^4 \odot^8$
IRAS 00091−0738	97 ± 1	2.30 ± 0.04	60^{+8}_{-7}	0.88 ± 0.10	0.57 ± 0.08	0.34 ± 0.04	98 ± 1	2.80 ± 0.03	62 ± 6	$\star^1$ − −
IRAS 00188−0856^a	93 ± 1	0.37 ± 0.04	37^{+6}_{-5}	<1.18	<0.67	<0.66	93 ± 1	0.42 ± 0.01	29^{+5}_{-4}	$\otimes^1 \odot^4$ −
IRAS 00456−2904	<1.0	−	<0.05	−	−	−	<1.0	−	<0.03	$\star^1$ − −
IRAS 00482−2721^b	<54	<0.04	<4.8	<0.01	$<0.96:$	$<0.79:$	<38	<0.07	<1.7	$\otimes^1$ − −
IRAS 01003−2238	96 ± 1	1.58 ± 0.02	53^{+6}_{-5}	0.18 ± 0.04	0.14 ± 0.01	<0.01	98 ± 1	2.12 ± 0.02	56^{+6}_{-5}	$\odot^1$ − −
IRAS 01166−0844	>99	$2.35^{+0.23}_{-0.08}$	89^{+6}_{-11}	$0.41^{+0.36}_{-0.33}$	$0.70^{+0.38}_{-0.35}$	$0.40^{+0.19}_{-0.18}$	>99	2.92 ± 0.04	90 ± 3	$\star^1$ − −
IRAS 01298−0744	>98	1.79 ± 0.02	77^{+5}_{-6}	0.91 ± 0.05	0.47 ± 0.03	0.29 ± 0.02	>99	2.29 ± 0.02	78 ± 5	$\star^1$ − −
IRAS 01569−2939	85 ± 1	$1.13^{+0.02}_{-0.04}$	19^{+5}_{-3}	$0.63^{+0.09}_{-0.07}$	0.31 ± 0.09	0.31 ± 0.05	91 ± 1	1.66 ± 0.05	22^{+5}_{-4}	$\star^1$ − −
IRAS 02021−2103	78 ± 2	1.91 ± 0.10	13^{+4}_{-3}	<0.01	$<0.40:$	$<0.18:$	86 ± 1	2.47 ± 0.11	15^{+4}_{-3}	− − −
IRAS 02411+0353^c	<17	−	<0.9	−	−	−	30 ± 2	0.77 ± 0.07	$1.2^{+0.4}_{-0.3}$	$\star^1$ − −
IRAS 03250+1606	<3.4	<0.11	<0.2	−	−	−	<3.9	<0.14	<0.2	$\otimes^1 \odot^4$ −
IRAS 04103−2838	59 ± 1	0.14 ± 0.02	$5.9^{+1.5}_{-1.1}$	<0.01	<0.01	<0.01	70 ± 1	0.63 ± 0.02	$6.3^{+1.6}_{-1.1}$	$\otimes^1$ − $\bullet^9$
IRAS 05189−2524	92^{+1}_{-3}	<0.01	32^{+6}_{-10}	<0.15	0.04 ± 0.01	<0.01	94 ± 1	0.43 ± 0.01	30^{+5}_{-4}	$\bullet^1 \bullet^4 \bullet^{10}$
IRAS 07598+6508^d	>99	<0.06	86 ± 4	<0.01	<0.01	<0.02	>97	<0.01	94^{+4}_{-44}	$\bullet^2 \bullet^4 \odot^{11}$
IRAS 08559+1053	68 ± 1	<0.01	$8.3^{+1.9}_{-1.4}$	<0.01	<0.16	$<0.12:$	65^{+1}_{-12}	<0.01	$5.0^{+1.2}_{-2.4}$	$\bullet^1 \bullet^4$ −
IRAS 08572+3915	>99	0.44 ± 0.01	87 ± 3	0.16 ± 0.02	0.24 ± 0.01	0.10 ± 0.01	>99	0.91 ± 0.01	81 ± 4	$\otimes^1 \bullet^4$ −
IRAS 09039+0503	61 ± 1	0.71 ± 0.04	$6.4^{+1.8}_{-1.3}$	<1.33	<0.01	$<0.38:$	72 ± 1	1.20 ± 0.04	$6.9^{+1.9}_{-1.3}$	$\otimes^1 \odot^4$ −
IRAS 09116+0334	<1.8	−	<0.08	−	−	−	<0.9	−	<0.03	$\otimes^1 \odot^4$ −
IRAS 09539+0857	91 ± 1	1.85 ± 0.03	30^{+6}_{-4}	<1.27	0.31 ± 0.03	0.28 ± 0.02	94 ± 1	2.38 ± 0.03	33^{+6}_{-5}	$\otimes^1 \star^4$ −
IRAS 10190+1322	<0.3	−	<0.02	−	−	−	<0.3	−	<0.01	$\star^1 \star^4$ −
IRAS 10378+1109	80 ± 1	0.21 ± 0.02	15^{+4}_{-3}	<2.56	0.43 ± 0.03	0.48 ± 0.03	87 ± 1	0.70 ± 0.02	16^{+4}_{-3}	$\otimes^1 \odot^4$ −
IRAS 10485−1447	60 ± 1	0.16 ± 0.03	$6.2^{+1.7}_{-1.2}$	<2.00	0.50 ± 0.07	$<0.34:$	70 ± 1	0.61 ± 0.04	$6.2^{+1.7}_{-1.2}$	$\otimes^1 \odot^4$ −
IRAS 10494+4424	<0.4	−	<0.02	−	−	−	<0.4	−	<0.01	$\otimes^1 \odot^4$ −
IRAS 11095−0238	97 ± 1	1.56 ± 0.01	63 ± 5	0.45 ± 0.02	0.59 ± 0.02	0.38 ± 0.01	98 ± 1	$2.05^{+0.08}_{-0.04}$	62^{+11}_{-8}	$\otimes^1 \star^4$ −
IRAS 11130−2659	84 ± 1	1.15 ± 0.02	19^{+4}_{-3}	0.37 ± 0.05	0.70 ± 0.05	0.40 ± 0.07	90 ± 1	1.67 ± 0.02	21 ± 4	$\otimes^1$ − −
IRAS 11387+4116	<0.8	−	<0.04	−	−	−	<0.7	−	<0.02	$\star^1 \star^4$ −
IRAS 11506+1331	54^{+1}_{-21}	<0.01	$4.9^{+1.3}_{-3.1}$	<0.29	$0.32^{+0.02}_{-0.20}$	<0.01	57 ± 1	0.18 ± 0.02	$3.6^{+0.9}_{-0.7}$	$\star^1 \odot^4$ −
IRAS 12072−0444	95 ± 1	1.07 ± 0.01	43^{+6}_{-5}	0.28 ± 0.02	0.26 ± 0.01	0.19 ± 0.01	97 ± 1	1.58 ± 0.01	45^{+6}_{-5}	$\bullet^1 \bullet^4$ −
IRAS 12112+0305	<13	<0.07	<0.7	−	−	−	<9.7	<0.04	<0.4	$\otimes^1 \star^5 \star^{12}$
IRAS 12127−1412^e	>99	<0.04	89^{+3}_{-4}	<0.44	<0.40	<0.38	>99	0.37 ± 0.01	84^{+3}_{-4}	$\otimes^1 \bullet^4$ −
IRAS 12359−0725	54^{+2}_{-43}	<0.01	$4.9^{+1.6}_{-4.4}$	<0.37	<0.48	<0.38	53^{+1}_{-8}	<0.01	$3.1^{+0.8}_{-1.2}$	$\otimes^1 \odot^4$ −
IRAS 13335−2612	<0.6	−	<0.03	−	−	−	<0.5	−	<0.02	$\otimes^1$ − −
IRAS 13454−2956	61^{+1}_{-27}	<0.01	$6.3^{+1.8}_{-4.5}$	<0.01	$<0.16:$	$<0.09:$	59 ± 1	0.07 ± 0.04	$4.0^{+1.1}_{-0.8}$	$\bullet^1$ − −
IRAS 13509+0442	<0.6	−	<0.03	−	−	−	<0.6	−	<0.02	$\star^1 \star^4$ −
IRAS 13539+2920	<0.4	−	<0.02	−	−	−	<0.4	−	<0.02	$\star^1 \star^4$ −
IRAS 14060+2919	<0.4	−	<0.02	−	−	−	<0.4	−	<0.01	$\star^1 \star^4$ −
IRAS 14197+0813^f	75 ± 2	2.10 ± 0.14	12^{+4}_{-3}	<1.61	<0.01	<0.01	84 ± 2	2.63 ± 0.15	13^{+4}_{-3}	− − −
IRAS 14252−1550	<20	<0.04	<1.1	−	−	−	<24	<0.31	<0.9	$\otimes^1 \star^4$ −
IRAS 14348−1447	51^{+3}_{-5}	<0.09	$4.3^{+1.7}_{-1.3}$	<1.94	$0.57^{+0.32}_{-0.36}$	$0.62^{+0.18}_{-0.26}$	59 ± 3	0.25 ± 0.10	$3.9^{+1.5}_{-1.0}$	$\otimes^1 \star^5 \star^{12}$
IRAS 15130−1958	91^{+1}_{-3}	<0.01	32^{+6}_{-10}	<0.08	<0.01	<0.01	94 ± 1	0.42 ± 0.01	30^{+5}_{-4}	$\bullet^1 \bullet^4$ −
IRAS 15206+3342	52 ± 1	0.30 ± 0.02	$4.5^{+1.2}_{-0.8}$	<0.01	<0.01	<0.01	65 ± 1	0.83 ± 0.02	$5.1^{+1.3}_{-0.9}$	$\star^1 \star^4$ −
IRAS 15225+2350	87 ± 1	0.74 ± 0.02	22^{+5}_{-3}	0.92 ± 0.05	0.35 ± 0.02	0.22 ± 0.01	92 ± 1	1.26 ± 0.02	24^{+5}_{-4}	$\star^1 \odot^4$ −
IRAS 15250+3609	96 ± 1	1.06 ± 0.01	53 ± 6	1.38 ± 0.03	0.60 ± 0.03	0.41 ± 0.02	98 ± 1	1.58 ± 0.01	55^{+6}_{-5}	$\otimes^2$ − $\star^{12}$
IRAS 15462−0450	90^{+1}_{-16}	<0.01	28^{+7}_{-19}	<0.01	$<0.07:$	$0.09^{+0.01}_{-0.05}$	89 ± 1	0.22 ± 0.01	19^{+4}_{-4}	$\bullet^1 \bullet^4$ −
IRAS 16090−0139	89 ± 1	0.69 ± 0.01	26 ± 4	0.90 ± 0.03	0.57 ± 0.02	0.36 ± 0.01	93 ± 1	1.21 ± 0.01	28^{+5}_{-4}	$\otimes^1 \odot^4$ −

Table 3 – *continued*

Source	α_6	τ_6	α_{bol}	τ_{ice}	$\tau_{HAC,1}$	$\tau_{HAC,2}$	$\alpha_6{}^*$	$\tau_6{}^*$	$\alpha_{bol}{}^*$	$V/L/X$
IRAS 16156+0146	94 ± 1	0.61 ± 0.02	43^{+6}_{-5}	0.48 ± 0.04	0.24 ± 0.01	0.11 ± 0.01	96 ± 1	1.09 ± 0.01	43^{+6}_{-5}	•[1] – –
IRAS 16468+5200	85 ± 1	0.77 ± 0.02	20^{+4}_{-3}	<1.50	0.94 ± 0.08	0.60 ± 0.04	91 ± 1	1.30 ± 0.02	22^{+5}_{-3}	⊗[1] ★[4] –
IRAS 16474+3430	<4.9	–	<0.3	–	–	–	<5.5	<0.01	<0.2	★[1] ⊙[4] –
IRAS 16487+5447[g]	21^{+1}_{-3}	<0.04	1.2 ± 0.4	–	–	–	31 ± 2	0.47 ± 0.08	$1.2^{+0.5}_{-0.3}$	⊗[1] ⊙[4] –
IRAS 17028+5817	<1.2	–	<0.06	–	–	–	<1.1	–	<0.04	⊗[1] ⊙[4] –
IRAS 17044+6720	91 ± 1	0.32 ± 0.01	29^{+5}_{-4}	0.09 ± 0.02	<0.01	<0.01	94 ± 1	0.82 ± 0.01	31^{+5}_{-4}	⊗[1] •[4] –
IRAS 17179+5444	84 ± 1	0.31 ± 0.02	18^{+4}_{-3}	<0.01	<0.01	<0.01	89 ± 1	0.81 ± 0.02	19^{+4}_{-3}	•[1] •[4] –
IRAS 17208−0014	<7.9	–	<0.4	–	–	–	<7.5	–	<0.3	⊗[3] ★[5] ★[12]
IRAS 19254−7245[h]	89 ± 1	0.21 ± 0.08	26^{+6}_{-5}	$0.21^{+0.17}_{-0.16}$	0.21 ± 0.04	0.10 ± 0.02	88 ± 1	0.09 ± 0.01	17 ± 3	•[3] •[5] •[12]
IRAS 20100−4156	86 ± 1	0.47 ± 0.02	22 ± 4	<2.44	0.77 ± 0.05	0.67 ± 0.03	92 ± 1	1.00 ± 0.02	24^{+5}_{-3}	★[3] ★[5] ⊙[12]
IRAS 20414−1651	<2.2	<0.07	<0.1	–	–	–	<2.7	<0.05	<0.08	★[1] ★[4] –
IRAS 20551−4250	90 ± 1	1.19 ± 0.01	28^{+5}_{-4}	0.38 ± 0.02	0.35 ± 0.01	$<0.09:$	94 ± 1	1.71 ± 0.01	31^{+5}_{-4}	⊗[3] •[5] •[12]
IRAS 21208−0519	<0.9	–	<0.04	–	–	–	<0.8	–	<0.03	★[1] ★[4] –
IRAS 21219−1757	>95	<0.01	85^{+11}_{-42}	<0.01	<0.01	<0.01	>98	0.37 ± 0.01	65 ± 5	•[1] •[4] –
IRAS 21329−2346	43 ± 2	<0.07	$3.1^{+1.0}_{-0.7}$	<1.08	<0.01	<0.01	55 ± 2	0.50 ± 0.05	$3.1^{+1.0}_{-0.7}$	⊗[1] ⊙[4] –
IRAS 22206−2715	<9.3	<0.17	<0.5	–	–	–	<11	<0.15	<0.4	★[1] – –
IRAS 22491−1808	<1.4	–	<0.07	–	–	–	<1.3	–	<0.04	★[1] – ★[12]
IRAS 23128−5919	48 ± 1	0.36 ± 0.03	$3.9^{+1.1}_{-0.8}$	<0.01	<0.01	<0.01	61 ± 1	0.87 ± 0.03	$4.3^{+1.2}_{-0.8}$	⊙[3] •[5] ⊙[12]
IRAS 23234+0946	30^{+2}_{-3}	<0.05	$1.8^{+0.6}_{-0.5}$	$0.31^{+0.07}_{-0.18}$	<0.01	<0.01	41 ± 2	0.47 ± 0.08	$1.9^{+0.7}_{-0.5}$	⊗[1] ★[4] –
IRAS 23327+2913	73 ± 1	0.86 ± 0.03	11 ± 2	0.11 ± 0.08	<0.01	$<0.26:$	82 ± 1	1.37 ± 0.03	11^{+3}_{-2}	⊗[1] ★[4] –
MRK 231	93 ± 1	<0.12	36^{+5}_{-4}	<0.17	0.08 ± 0.01	0.03 ± 0.01	97 ± 1	0.68 ± 0.01	51^{+6}_{-5}	•[2] •[4] •[12]
MRK 273	67^{+1}_{-4}	<0.01	$8.1^{+1.9}_{-1.3}$	$0.55^{+0.01}_{-0.14}$	$0.49^{+0.02}_{-0.09}$	$0.17^{+0.01}_{-0.03}$	76 ± 1	0.45 ± 0.01	$8.4^{+2.0}_{-1.4}$	•[1] •[4] •[13]
NGC 6240	65^{+6}_{-8}	$0.64^{+0.20}_{-0.24}$	$7.5^{+4.0}_{-3.0}$	<0.01	<0.01	<0.01	76^{+3}_{-6}	1.15 ± 0.18	$8.1^{+3.6}_{-2.8}$	⊗[2] •[6] •[14]
4C+12.50	97 ± 1	0.24 ± 0.02	62 ± 7	0.11 ± 0.04	<0.01	0.05 ± 0.01	98 ± 1	0.74 ± 0.02	63 ± 7	•[1] •[4] •[11]
UGC 5101[i]	81^{+1}_{-3}	<0.02	16 ± 3	<1.06	<0.99	<0.90	83 ± 1	0.19 ± 0.01	13^{+3}_{-2}	⊗[2] •[7] •[15]

References. [1]Veilleux et al. (1999a), [2]Veilleux et al. (1995), [3]Duc et al. (1997), [4]Imanishi, Dudley & Maloney (2006), [5]Risaliti et al. (2006b), [6]Risaliti et al. (2006a), [7]Imanishi, Dudley & Maloney (2001), [8]Iwasawa et al. (2005), [9]Teng et al. (2008), [10]Severgnini et al. (2001), [11]Imanishi & Terashima (2004), [12]Franceschini et al. (2003), [13]Balestra et al. (2005), [14]Vignati et al. (1999), [15]Imanishi et al. (2003).
Note. [a]The value of τ_6 is obtained allowing $\Gamma_{AGN} = 0.78$. [b]This is indeed considered an AGN detection. [c]A comparable minimum in the parameter space suggests a possible AGN component with $\tau_6 = 0.24$ and $\alpha_{bol} = 1.1$ (per cent). [d]The value of τ_6 is obtained allowing $\Gamma_{AGN} = 0.58$. [e]The value of τ_6 is obtained allowing $\Gamma_{AGN} = 1.31$. [f]A comparable minimum in the parameter space suggests that this source could also be SB-dominated. [g]Due to the dispersion around the templates, this value of α_{bol} is too small to include this source among the safe AGN detections. [h]The value of τ_6 is obtained allowing $\Gamma_{AGN} = 0.52$. [i]The value of τ_6 is obtained allowing $\Gamma_{AGN} = 1.02$.

for each source the following quantities:

$$\widehat{R}^{AGN} = \left(\frac{\nu_6 \alpha_6 f_6^{int}}{\alpha_{bol} F_{IR}} \right) \quad \text{and} \quad \widehat{R}^{SB} = \left[\frac{\nu_6 (1 - \alpha_6) f_6^{int}}{(1 - \alpha_{bol}) F_{IR}} \right]. \quad (6)$$

Although this argument may appear as fully circular, it indeed provides a strong confirmation of our approach. In fact, as shown in Fig. 4(b), the ratios $\widehat{R}^{SB}$ for the SB component in composite sources (which depend on our AGN/SB decomposition) agree within the dispersion with those for SB-dominated ULIRGs (which conversely are directly measured). Such agreement would be lost both in case of missed AGN detections and in case of fake AGN detections, since the global IR flux is sensitive to the actual AGN contribution.

The present method is then reliable in detecting genuine AGN components and in extrapolating the average AGN/SB contribution to the bolometric luminosities. Moreover, in spite of its simplicity, it proves to be effective when compared to other diagnostics at different wavelengths, as discussed in the next section. It is important, however, to underline that the scatter in $\widehat{R}^{AGN}$ and $\widehat{R}^{SB}$ is significantly larger than the uncertainty on the best values of R^{AGN} and R^{SB}. The reduced χ^2 of the R–α_6 relation varies slowly within a

region of the parameter space that roughly corresponds to the dispersion around the best fit in Fig. 4(a). We then emphasize that such a dispersion (~0.3 dex, nearly constant with respect to α_{bol}) is to be considered the real uncertainty in the 6 μm to bolometric ratios for the AGN and SB components of individual objects (as opposed to the ensemble averages). This can slightly affect the estimates of α_{bol}, increasing the statistical errors reported in Table 3 as well. Nevertheless, the results are precise enough to establish the magnitude of the AGN/SB contribution both to the luminosity of individual sources and to the overall energy output of local ULIRGs.

In the light of the elements collected so far, we are able to address again the question about the existence of extremely obscured AGN components that cannot be detected even at 5–8 μm, but only contribute to the IR emission at longer wavelengths (e.g. at ~25–60 μm). Such components would pull downwards our estimate of $\log R^{SB} = -1.91$. An empirical measure of this quantity can be performed at lower IR luminosities on the B06 SB sample, yielding an average of $\log R^{SB} = -1.66$. This latter value anyway requires some caution for two opposite reasons: some objects in B06 (e.g. NGC 1365, NGC 4945) show significant nuclear activity; on the other hand, we are dealing with nearby sources and aperture losses
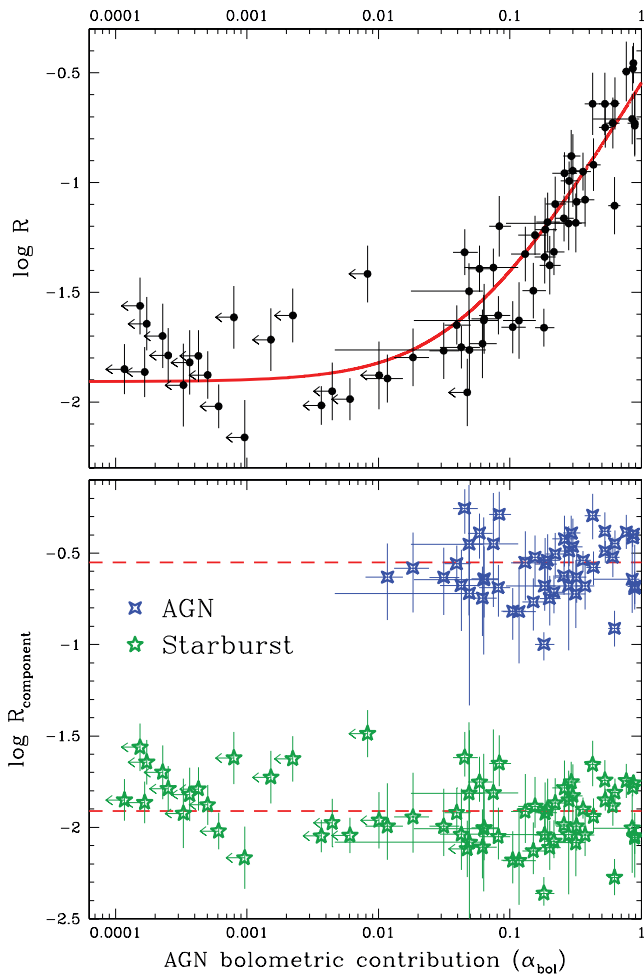
Figure 4. (a) Ratio R between intrinsic 6 µm and bolometric luminosity versus the AGN bolometric contribution α_{bol}. The error bars of R are mainly due to the uncertainties in the total IR flux F_{IR}. The red solid curve traces the best fit of the R–α_6 relation from equation (4). It is worth noting that the sources follow a very regular pattern and no evidence of outliers is found. (b) Same as above, with the ratios for the AGN and SB components plotted separately. The red dashed lines mark the best values of R^{AGN} and R^{SB}. The agreement among the SB components at different values of α_{bol} proves the reliability of our method (see the discussion in the text).

in the SL spectral orders can occur.[5] Disregarding such complications (these systematic effects are believed to compensate for each other), it turns out that the two distributions of R^{SB} fairly overlap, due to their large dispersion. Even if they appear to be somewhat displaced with respect to each other, the variation is too small to support the hypothesis of a completely buried AGN population escaping this 5–8 µm spectral probe (or any other *Spitzer*–IRS probe; see also Veilleux et al. 2009). This difference can be possibly ascribed to the overall physical properties of the SB process itself; for example, in the ULIRG luminosity range the SB is triggered by a major merger (e.g. Dasyra et al. 2006), while at lower luminosities it mostly takes place in isolated systems.

---

[5] We have adopted the same strategy of B06, scaling up all the spectral orders to match the LL1 flux density, and then normalizing to *IRAS* at 25 µm. By comparing the final spectra to the 12 µm *IRAS* fluxes, we evince that a residual loss may be present, and provide an upper limit for the average of $\log R^{SB} \approx -1.5$.

7 COMPARISON WITH OTHER DIAGNOSTICS

Our 5–8 µm AGN/SB decomposition has provided 50 convincing AGN detections out of 71 sources in our sample, confirming all the already known AGN components and uncovering some more. Conversely, the AGN detection rate among ULIRGs is ∼30 per cent at optical wavelengths (Veilleux et al. 1999a), and <50 per cent according to mid-IR high-ionization lines (Farrah et al. 2007). X-ray diagnostics are actually extremely powerful, but can be applied on such a large scale only collecting a huge integration time: after Teng et al. (2005), we estimate that an average exposure of ∼30 ks per source is required in order to reach up to our detection rate with the present X-ray facilities. In Section 2, we have briefly summarized the multiwavelength picture of ULIRGs which is obtained from the most effective diagnostic methods used so far. We now discuss in more detail how our results compare with those of previous works, allowing us also to overcome some of their limitations.

7.1 Optical

The nuclear regions of ULIRGs are affected by typical obscurations of several tens of magnitude at visible wavelengths, hence it is difficult to interpret the results of the diagnostics based on emission lines. None the less, some ULIRGs exhibit in their spectra the broad optical recombination lines characteristic of Seyfert 1 galaxies. Even when a direct access to the broad-line region is obstructed by larger amounts of dust, possibly aggregated in a toroidal shape as expected for type 2 Seyfert-like objects, the presence of a working AGN can be firmly established in the near-IR via the detection of broad permitted features or of the high-ionization 1.962 µm [Si VI] line (Veilleux, Sanders & Kim 1999b). In principle, a hidden broad-line region can also be looked for in the polarized light, a technique that has been developed with success for nearby Seyfert 2 galaxies (after Antonucci & Miller 1985) but is almost unavailable for ULIRGs (e.g. Pernechele et al. 2003) because of their larger distance, and possibly frustrated by the greater complexity in the geometrical structure of the dust (large covering factors and clumpiness are not easily reconcilable with the reflection scenario, nor with dichroic transmission). In most cases, only narrow features are observed, and it is necessary to resort to line ratios in order to classify a ULIRG. The separation of active nuclei and star-forming galaxies is based on empirical boundaries, discriminating the effects of photoionization by hot young stars from those due to non-thermal sources with a power-law continuum. This is in itself a limitation to the accuracy of this diagnostic method, which is further degraded by the extinction effects. According to Veilleux & Osterbrock (1987), three equivalent diagnostic diagrams can be set up using the line ratios [O I] λ6300/Hα, [N II] λ6583/Hα and [S II] (λ6716+λ6731)/Hα along with [O III] λ5007/Hβ (the latter distinguishes between a type 2 Seyfert galaxy and a LINER). It turns out that a significant number of ULIRGs do not belong to the same spectral type in all these diagrams, with some degree of overlap among LINERs and H II regions (Veilleux et al. 1999a). In any case, no evidence of AGN activity is clearly found within these two classes.

In Fig. 5, the AGN intrinsic contribution to the 5–8 µm emission and its obscuration, as obtained with our technique, are plotted together with the optical properties. With some scatter, the location of each source correlates with its optical classification. In particular, there is a tight agreement for Seyfert-like ULIRGs: type 1 objects are found in the bottom-right corner, with a large AGN content
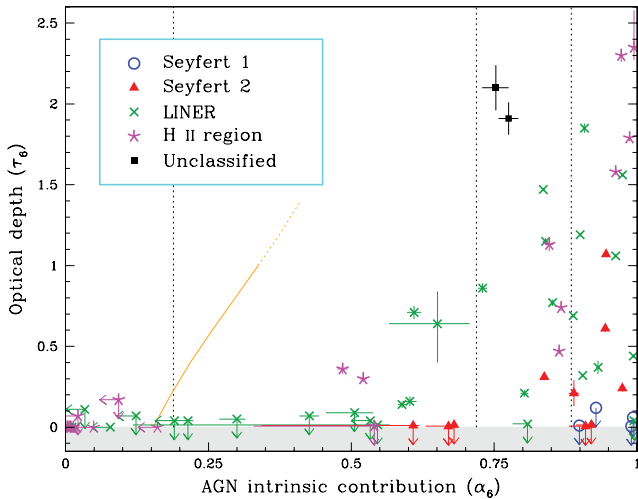
Figure 5. Optical depth to the AGN component evaluated at 6 μm versus the AGN intrinsic contribution to the 5–8 μm emission. Each source is plotted with a different symbol according to its optical classification, as indicated in the box. The vertical black dotted lines mark an AGN contribution to the bolometric luminosity of 1, 10 and 25 per cent, respectively. The crosswise orange curve represents our empirical detection limit: due to the dispersion around our AGN/SB templates, an AGN component on the left of this line could be missed by our method (because its observed contribution is too faint). For the same reason, AGN detections close to this region of the plot are to be considered as tentative. The bolometric contribution of such components would be anyway negligible (a few per cent at most).

and vanishing obscuration, while the average type 2 hosts a slightly dimmer and obscured AGN. The interpretation of the plot is less straightforward when one also considers the sources that are classified as H II regions or LINERs. It is clear that optical spectroscopy, besides giving incomplete information about the relative AGN/SB contribution, can also be misleading: this is indicated by the presence of only one type 2 Seyfert-like source among the nine entries with $\alpha_{bol} > 0.25$ and $\tau_6 > 1$. Also, four H II galaxies fall into this group, and they are all true AGN detections at a simple visual inspection, sharing a reddened and absorbed continuum and strongly suppressed aromatic features. These targets are hence perfect candidates for follow-up observations at X-ray wavelengths. As opposed to the unexpected scatter of H II galaxies, the wide dispersion of LINERs in Fig. 5 confirms again that such systems are rather heterogeneous with respect to the nature of their energy source. Out of 33 LINERs comprised in our sample, 23 contain an AGN component, with a wide range of bolometric contributions. This fraction (~70 per cent) is very close to the detection rate achieved by collecting all multiwavelength diagnostics, but is significantly higher than those obtained from radio, optical and X-ray observations separately. Our decomposition method is then capable to resolve most of the ambiguity concerning the ionization mechanism in LINERs (see also Dudik, Satyapal & Marcu 2009; Gonzalez-Martin et al. 2009).

7.2 Mid-IR

A wealth of studies at mid-IR wavelengths have been published since the launch of the Infrared Space Observatory (ISO; Kessler et al. 1996), most of which rely on different mixtures of three basic diagnostics, i.e. hot dust continuum, aromatic emission and silicate absorption. The usual strategy makes use of single indicators

such as the equivalent width of the 6.2 or 7.7 μm PAH feature, flux ratios involving fine-structure lines, the 9.7 μm silicate optical depth, the 15 to 6 μm continuum colour. Pairs of these diagnostics are used to construct two-dimensional diagrams in which the location of ULIRGs is compared with those of standard AGN and SB control samples (e.g. Genzel et al. 1998). Alternatively, one can attempt at reproducing the whole observed emission within a certain wavelength range by means of a limited number of components. Both spline continua plus variable PAH emission and fixed spectral templates have been employed. Our method follows the latter approach, and is qualitatively similar to those presented in Laurent et al. (2000) and Tran et al. (2001), with the great improvement in data quality made available by *Spitzer*. It is difficult to find a quantitative correspondence among the results obtained on the individual objects, since these earlier works were intended primarily to derive the statistical properties of the ULIRG population as a whole. A possible example of a more specific comparison is illustrated in Fig. 6, where the AGN observed contribution to the 5–8 μm emission of 48 sources is compared to the equivalent widths of the 6.2 and 7.7 μm aromatic features (from Veilleux et al. 2009). The expected anticorrelation between these quantities can be appreciated, and the scatter is highly reduced with respect to the measurements performed before the *Spitzer* era (e.g. Rigopoulou et al. 1999). At the same time, it is clear that reddening extensively shapes the spectra of ULIRGs, and its effects have a substantial impact when estimating the AGN/SB bolometric contribution.

Another way to probe the degree of absorption and the geometrical structure of the dust, and test the characterization we offer of these issues, is provided by the silicate feature at 9.7 μm: its opacity, together with the intensity of aromatic emission, can be plotted in a diagram useful not only for working as a classification scheme but also for tracing the possible evolutionary path of a source. The silicate feature has not been studied in the present work. We anyway point out the good agreement between our findings about the most notable sources in our sample and their position in such a diagnostic diagram (Spoon et al. 2007). In particular, the silicate strength appears to have a positive correlation with the reddening we have estimated for the AGN component.
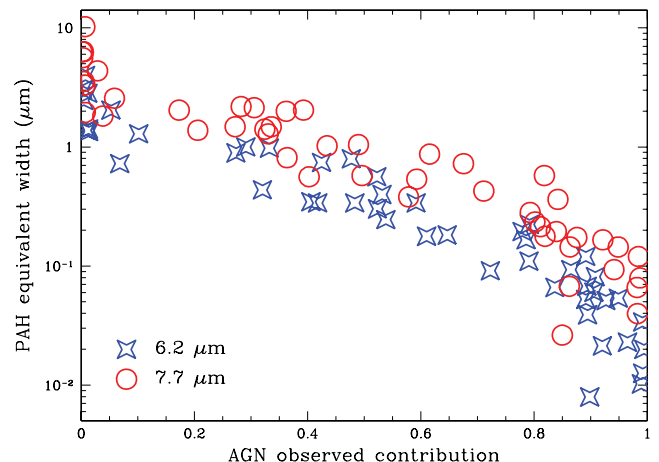
Figure 6. Equivalent widths of the 6.2 μm (blue diamonds) and the 7.7 μm (red rings) PAH features (from Veilleux et al. 2009) plotted against our estimate of the AGN observed contribution to the 5–8 μm continuum, evaluated at the same wavelength. The typical error bars are comparable to the symbol size.

7.3 High-ionization lines

As mentioned before in relation with the 1.962 μm [Si VI], the presence of fine-structure lines from highly ionized atoms has a powerful diagnostic value in distinguishing between black hole accretion and star formation in ULIRGs. Also in the mid-IR, the mere detection of features such as the [Ne V] λ14.32 line is the clear mark of an active nucleus, because of the required ionization energy of 97.1 eV. Again, by combining suitable line ratios among themselves or with different AGN/SB indicators, useful diagnostic diagrams can be set up, that make it possible to point out the main average trends but can be misleading if applied to single objects.

Recently, Farrah et al. (2007) have analysed the high-resolution *Spitzer*–IRS spectra of 53 local ULIRGs, 27 of which are also included in our sample. This allows a meaningful comparison between our AGN/SB decomposition method and diagnostics based on fine-structure lines. Focusing on the common sources, three of them have been used for the construction of our SB template, while signatures of AGN activity have been found in each of the remaining 24 according both to Paper I and the present work. We therefore look for a confirmation of this activity through high-ionization lines. The simplest approach is of course the detection of individual features. [Ne V] λ14.32 is found in 10 objects, in nine of which we detect an AGN component as well. The only exception is IRAS 20414−1651 that we have assumed to be a prototypal SB because of its prominent PAH features and cold mid-IR colours. IRAS 20414−1651 is actually the only case without the simultaneous detection of [O IV] λ25.89, another usual clue of hard radiation fields. On the contrary, IRAS 10378+1109 tentatively shows the oxygen line but no neon emission.[6] It is not obvious to relate the absence of [Ne V] λ14.32 to a higher degree of obscuration. Both MRK 231 and IRAS 15462−0450, for instance, are not detected in [Ne V] λ14.32 despite their nature of type 1 Seyfert galaxies at optical wavelengths. The same holds for IRAS 07598+6508. None the less, it is worth noting that the median value of the optical depth to the AGN component is ∼0.3 for the nine ULIRGs with a [Ne V] λ14.32 detection and ∼0.5 for the remaining 15 composite sources, and indeed the argument of a larger obscuration seems to be reasonable for many of them. A high covering factor of the absorbing dust can even prevent the formation of a narrow-line region and the production of fine-structure lines. A complete revision of both line fluxes and upper limits can be found in the recent work of Veilleux et al. (2009) that also includes 25 additional sources within our sample. The considerations made so far are widely corroborated. There are six more objects with a [Ne V] λ14.32 line: only one (IRAS 13335−2612) is classified as SB-dominated after our 5–8 μm spectral analysis. Also, the loose correlation between successful detections and little opacities is possibly emphasized.

The line ratios allow more complete diagnostics in combination with some other AGN/SB indicator over the electromagnetic spectrum. All the diagrams proposed by Farrah et al. (2007) point to star formation as the dominant power supply in ULIRGs: the active nucleus is as powerful as the SB in only ∼20 per cent of the sources, and of lesser significance in more than half. These fractions are in perfect agreement with our estimates. The effectiveness of mid-IR fine-structure lines in ULIRG diagnostics is anyway restricted to the finding of general trends, since no firm quantitative constraint

can be put on the AGN bolometric contribution (except for some remarkable examples), and even qualitative considerations may lead to mistaken conclusions on individual objects.

7.4 Hard X-rays

Since ULIRGs are faint X-ray emitters, with a 2–10 keV continuum flux ranging from ∼10^{-5} to a few ×10^{-3} of their overall IR output, only a limited number of them have been observed successfully with the *Chandra* and *XMM–Newton* satellites. We can therefore provide only a brief compilation of the main results that have been obtained so far. Clear X-ray signatures of AGN activity are a 2–10 keV luminosity exceeding 10^{42} erg s^{-1} and a large column density ($N_H > 10^{22}$ cm^{-2}) absorbing an unresolved component. The detection of the iron Kα fluorescent line at 6.4 keV with an equivalent width of ∼1 keV also indicates the presence of an obscured active nucleus, whose primary radiation is reflected by a *cold* mirror of gaseous material (for a detailed review about this subject, see Reynolds & Nowak 2003). All these indicators have been found in IRAS 19254−7245 (Braito et al. 2003, 2009). MRK 231 lacks a strong iron line, but the direct AGN emission emerges above 20 keV (Braito et al. 2004); moreover, this source exhibits significant nuclear variability on time-scales of a few hours (Gallagher et al. 2002). Both nuclei of NGC 6240 have hard X-ray emission that possibly dominates the global energetics, with heavy absorption and a prominent neutral iron line (Vignati et al. 1999; Komossa et al. 2003). IRAS 05189−2524 is a typical Compton-thin Seyfert 2 galaxy, in which the estimated luminosity of the AGN component cannot account for the huge IR emission (Severgnini et al. 2001); also MRK 273 (Balestra et al. 2005) and UGC 5101 (Imanishi et al. 2003) are likely SB-dominated, although an AGN is detected above ∼3–4 keV. The hard X-ray luminosity and spectral properties suggest an AGN contribution to IRAS 20551−4250 and, tentatively, to IRAS 23128−5919 and IRAS 20100−4156, while no convincing evidence of AGN is found in IRAS 12112+0305, IRAS 14348−1447, IRAS 15250+3609, IRAS 17208−0014 and IRAS 22491−1808 (Franceschini et al. 2003; Ptak et al. 2003).

Even when measured, the luminosity of the above-mentioned AGN components generally lies in the range of Seyfert galaxies. In order to represent the major energy source of the ULIRG bolometric luminosity, they should be located behind a column density of obscuring material approaching 10^{25} cm^{-2}. It is still matter of debate if this is the case for ARP 220, the nearest ULIRG, inside which an elusive active nucleus is suspected to be at work. A strong iron line has indeed been detected in ARP 220 by Iwasawa et al. (2005), challenging the origin of the 2–10 keV emission from X-ray binaries and hence the pure SB interpretation (for the X-ray emission processes in SB galaxies, see Persic & Rephaeli 2002).

A handful of additional sources has been recently studied by Sani, Risaliti & Salvati (in preparation) using also the *BeppoSAX* observations up to 100 keV. The most striking result concerns IRAS 12072−0444, which is detected only at energies beyond 20 keV and shows up as a Compton-thick source harbouring a type 2 quasar with a column density $N_H \simeq 4 \times 10^{24}$ cm^{-2}. IRAS 08572+3915 is not detected but is suggested to be a type 2 quasar as well, whose reflection efficiency is very low by virtue of a cocoon-like obscuring geometry. Finally, on the basis of the ratio between the 2–10 keV and the IR emission, IRAS 10190+1322 and IRAS 10494+4424 confirm their SB-dominated nature, while the presence of an AGN component cannot be ruled out in IRAS 00188−0856, IRAS 01003−2238 and IRAS 16090−0139: according to their *Spitzer*–IRS spectra and the findings of the present work, these latter objects are believed to

---

[6] This detection is not actually confirmed by Veilleux et al. (2009), as well as the detections in 4C +12.50; the [Ne V] λ24.32 line is instead found in IRAS 15206+3342.

host a buried AGN and are expected to be absorbed even at 10 keV. Regrettably one of them (IRAS 16090−0139) was observed but not detected by *BeppoSAX*, and the upper limit to its flux above 20 keV is not constraining; the other two have not been observed at all.

In conclusion, our results are in qualitative agreement with all the pieces of evidence from X-ray studies. The X-ray diagnostics of ULIRGs are very powerful, yet our 5–8 μm analysis provides fully consistent indications and, at present, gives access to a much larger number of sources.

8 DISCUSSION

Having illustrated the global results of our study and their consistence with the multiwavelength picture of ULIRGs, in this section we discuss in quantitative terms the reliability of alternative AGN templates. We also address some uncertain or anomalous cases, and their consequences with respect to the dust properties within the ULIRG class. We finally investigate whether our analysis is able to recover the claimed correlation between AGN activity and bolometric luminosity.

8.1 Fitting of peculiar sources

In our model, the great diversity of the observed ULIRG spectra can be entirely ascribed to the relative amount of the AGN contribution and its obscuration, intended as both absorption and reddening. The main features are adequately reproduced, and a good fit is obtained for most of the spectra in our sample, with only a few exceptions whose analysis required additional assumptions. The main issue is the possible flattening of the AGN component (as found by N07), which entails a relaxation of our general template. The representative case is that of IRAS 07598+6508, which is unambiguously an AGN-dominated source: its continuum trend can be reproduced by simply allowing the AGN spectral index to be ∼0.6. IRAS 19254−7245 (the *Superantennae*) is instead a composite system with regular absorption features. In order to obtain a good fit, we again need to provide a flatter AGN component: including its intrinsic slope among the degrees of freedom we obtain a value of ∼0.5, with a 6 μm optical depth of ∼0.2.

The remaining three particular cases (that in the following will also be labelled as *anomalous*) are more interesting, in that the supplementary presence of a broad and deep absorption over most of the 5–8 μm range causes the failure of our continuum-based AGN/SB decomposition. All these objects are likely to host a completely buried AGN; their emission is shown in Fig. 7, where they are compared to the benchmark spectrum of IRAS F00183−7111 (Spoon et al. 2004; Nandra & Iwasawa 2007). Qualitatively, IRAS 12127−1412 is the most striking object in our sample, since the broad absorption completely replaces the 6.2 μm PAH emission (no trace of which is clearly visible) and stretches longwards of 7 μm. In IRAS 00188−0856 and UGC 5101, a strong, hard spectrum (closely resembling the hot dust continuum of AGN) stops abruptly: this occurs in some other sources as well, but the putative AGN continuum is rather steep and only a proper modelling of the absorption profiles is entailed. On the contrary, the three cases at issue suggest once again a flattening of the AGN component with respect to $\Gamma_{AGN} = 1.5$, and the aromatic features, if present, seem to emerge from the bottom of a deep trough. A customized fitting procedure is therefore needed. The observed continuum is assumed to be AGN-dominated at ∼5.5 μm, and since the available window is very narrow we have employed the 15 μm flux as a pivotal point of the fit. The AGN intrinsic slopes obtained in such way range from
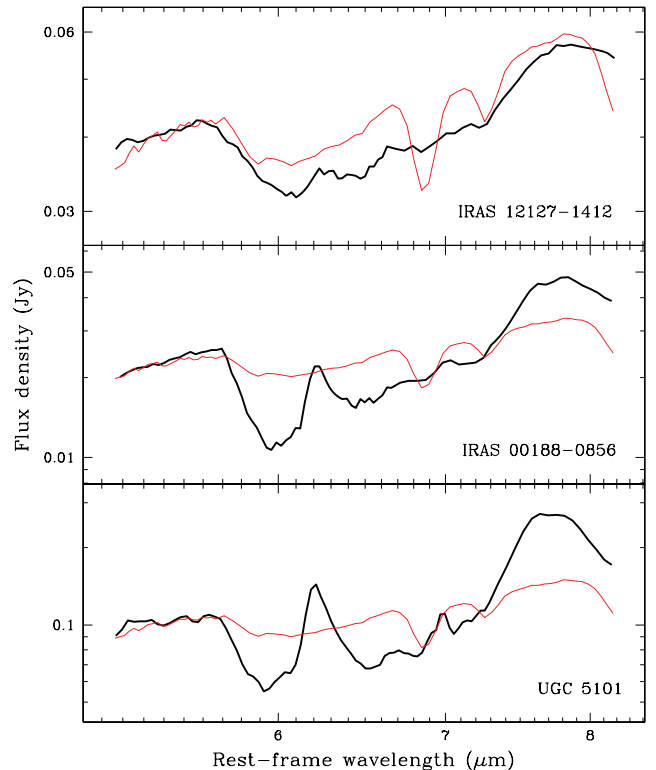
**Figure 7.** The puzzling spectral trend of the *anomalous* sources in our sample, compared to the 5–8 μm emission of IRAS F00183−7111 (thin red line, scaled to match the putative hot dust continuum). The apparent flatness can indeed be connected to extreme absorption of the AGN component within a different extinction scenario.

∼0.8 to ∼1.3, with τ_6 between ≃0.4 and ≃0. We have then frozen the continuum and included the SB component and the absorption profiles in the next fitting step. The silicate feature is also required longwards of ∼7.5 μm, as in other few objects. The physical interpretation of these *anomalous* spectra, concerning both flatness and extreme absorption, will be discussed in detail in the following sections.

8.2 The AGN intrinsic spectral slope

A power-law behaviour of the 5–8 μm hot dust continuum in AGN is confirmed by the observations, which however provide different values of the spectral index. We recall that the slope of the AGN template cannot be treated as a free parameter, because of its degeneracy with the optical depth. Our assumption of a steep intrinsic gradient has been explained in Section 3. Conversely, we have just presented a few peculiar cases whose spectra are better reproduced by a lower value of Γ_{AGN}. It is then worth testing how our estimates of the AGN bolometric contribution depend on this choice.

Since the quality of our fits is good and the SB template is not modified, we expect the observed AGN component to be nearly invariant. Hence, the flatter the intrinsic continuum, the larger the optical depth, and consequently the AGN flux amplitude. As a first approximation, the relative *weight* of the AGN component is then increased after the flattening of the intrinsic spectral shape. We have again performed the fitting of all our sources, modifying the AGN template and assuming the new value of $\Gamma_{AGN} = 0.7$ for its slope, as suggested by N07. The goodness of our fits remains virtually unchanged, and no convincing additional AGN detection is found.
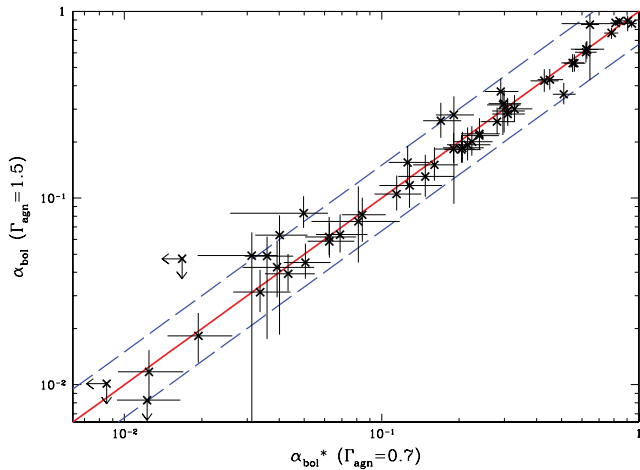
Figure 8. Different estimates of the AGN bolometric contribution (α_{bol} and α_{bol}^*) as a function of its intrinsic spectral slope. The vertical axis shows the values obtained for $\Gamma_{AGN} = 1.5$, the horizontal one those obtained for $\Gamma_{AGN} = 0.7$. The red solid line marks the equality between the two estimates, while the blue dashed lines indicate a deviation of 50 per cent: each entry falls inside this region. For clarity, 17 sources that are confirmed to be SB-dominated in both cases have been omitted, and fall outside the region plotted above. We recall that, due to the dispersion around our templates, safe AGN detections require $\alpha_{bol} \gtrsim 0.01$.

As forecast, however, both the optical depth and the AGN amplitude increase remarkably, because of the degeneracy between Γ_{AGN} and τ_6 connected to the assumed *recipe* for the extinction law. The systematically larger AGN flux also affects our estimate of R^{AGN}, from the fitting of the $R-\alpha_6$ relation of equation (4). The modified values of the 6 μm to bolometric ratios are the following:

$$\log R^{AGN} = -0.36^{+0.06}_{-0.07} \quad \text{and} \quad \log R^{SB} = -1.91^{+0.02}_{-0.02}.$$

With respect to the estimates of Section 6, R^{SB} is confirmed (the SB template is not changed), while R^{AGN} turns out to be ∼0.2 dex higher. The revised values of α_{bol} are again computed from equation (5), where now $R^{AGN}/R^{SB} \simeq 35$. A striking result is obtained as a consequence of the correlation between α_6 and R^{AGN}, i.e. a moderate variation in the slope of the AGN template has no significant effect on α_{bol}. This invariance can be better appreciated in Fig. 8, while Table 3 lists the two alternate values of both the AGN bolometric contribution and the optical depth. This is of course a notable finding. Nevertheless, we emphasize once again that our original template appears to be more suitable to describe the AGN component inside a ULIRG, in spite of the peculiar cases. The alternative scenario, in fact, implies that virtually all the detected AGN components are heavily reddened; as a consequence, the distribution of continuum opacities is discontinuous and strongly biased towards the highest values. This anomaly cannot be explained even allowing a far larger dispersion in the 5–8 μm AGN spectral shapes than that observed by N07.

8.3 Absorption features

We have already mentioned how the SB component is affected by internal extinction only; the large spread in the optical depth of the 9.7 and 18 μm silicate absorption features within the SB class suggests a wide range of dust properties, a full investigation of which would require a larger spectral coverage and a more detailed model than those considered in this work. Concerning the AGN component, it is not possible to put constraints on the nature or geometry

of the cold screen blocking the view to the nuclear region. However, we are able to discuss the properties of the main absorption features and the accuracy of a power-law extinction curve.

In general, the AGN and SB templates we have adopted are sufficient to account for all the major features observed in the 5–8 μm spectra of ULIRGs. Minor features, when involved, have been reproduced through Gaussian profiles, but do not alter the AGN/SB decomposition. There are indeed plenty of possible absorption features falling in the 5–8 μm range, as can also be inferred from the observations of a highly obscured environment like the Galactic Centre. Notably, none of these has been found in our spectra without the simultaneous detection of a significant AGN contribution to the continuum emission. A characteristic couple of features is frequently distinguished in composite sources, centred at ∼6.85 and ∼7.25 μm and ascribed to the C–H bending modes of aliphatic hydrocarbons [also known as hydrogenated amorphous carbons (HAC)]. They usually display a regular Gaussian profile, and their relative depth can be used to constrain the chemical properties of the dust grains (see also Dartois & Muñoz-Caro 2007). The most sensitive point for our study is anyway the possible presence of another absorption feature, centred at ∼6.0 μm, that is commonly attributed to a mixture of ices and is much more complex. Although this profile can be strongly asymmetrical, with an elongated red wing, it is usually so shallow and/or regular that a rigorous selection of its shape is not required. In the mentioned case of Sgr A*, the 6 μm feature would be optimally fitted by means of pure H_2O ice at 30 K (Chiar et al. 2000), and this consequently represents a reasonable modelling for our purposes. We therefore decided to adopt the pure water ice profile at 30 K (provided by the Leiden Observatory data base) as the backbone of the 6 μm absorption in our fits.

As discussed in the following, this assumption is challenged in only a few objects hosting a deeply enshrouded AGN (including the three *anomalous* spectra, where it actually fails). The plain identification in terms of water ice, in fact, would lead to a large overestimate of the optical depth in the companion 3 μm absorption band. A simultaneous fit of both profiles in Sgr A* drives only a partial explanation of the 6 μm feature as the product of a mixture of ices, i.e. $H_2O:NH_3:CO_2$ (100:30:6) at 15 K and pure HCOOH at 10 K (Chiar et al. 2000). Most of the residuals are accounted for by a 6.2 μm component whose origin is supposed to be aromatic. This remarkable example proves how the exact nature of the whole 6 μm feature is still poorly known. Yet the formation by surface chemistry of many different species in the icy mantles of the dust grains suggests the possibility of large variations in its profile, as a function of the chemical and physical properties of each source. This is indeed what we find out, since the central wavelength (actually the wavelength of minimum flux) appears to shift within the ∼5.9–6.2 μm range, and also the blue and red wings tend to be slightly different for the objects whose optical depth[7] (hereafter τ_{ice}) is larger than that of Sgr A*. A sizable value of τ_{ice} can be considered itself a qualitative indicator of a significant AGN contribution, but in extreme cases it can even prevent a straightforward AGN/SB decomposition.

In the light of the above considerations, a likely interpretation of the broad absorption band characterizing some of our 5–8 μm spectra is the blending of the 6 μm ice profile with the pair of

---

[7] All the optical depths concerning individual features refer to the AGN component only, and are evaluated considering the observed (i.e. not corrected for reddening) AGN continuum from the best fits.

HAC features around 7 μm. Evidence of a dramatic broadening of the 6.85 μm line is actually found in the observations of several embedded protostars (Keane et al. 2001). Moreover, according to a recent spectroscopic survey of young stellar objects, both water ice and HAC seem to play a deficient role among the carriers of the most enigmatic 5–8 μm depressions (Boogert et al. 2008). This could provide a physical explanation also to the spectral peculiarities observed in the three *anomalous* cases, in which the deviations from the standard ∼6 and 6.85 μm profiles give rise to a formless band that undermines our approach.

8.4 Absorption versus reddening

An accurate chemical analysis goes beyond the aims of the present work, anyway a further line of investigation can be pursued, involving the study of possible correlations between the optical depth of the most prominent absorption features and the reddening of the dust continuum. In Fig. 9, some representative ULIRG spectra have been arranged in a slope sequence with decreasing steepness with respect to the observed AGN component. Different colours have been used in order to flag the absorption degree and avoid ambiguities in

Figure 9. From top to bottom, the 5–8 μm spectra of the following sources are plotted in a slope sequence with decreasing steepness: (1) IRAS 01298−0744, (2) IRAS 20100−4156, (3) IRAS 16156+0146, (4) IRAS 00188−0856, (5) IRAS 08572+3915, (6) IRAS 21219−1757, (7) IRAS 12127−1412 and (8) UGC 5101. Colours are used to denote the consequence of absorption (red, green, blue and black in the order of growing significance). This contrast shows the wide variety in both reddening and absorption characteristic of ULIRGs.

the following considerations. Through a simple comparison among the adjacent spectra, it is clear that the intensity of the absorption features varies considerably within the same range of continuum slope. The effects of extreme absorption are evident, for example, in the *black* spectra (IRAS 20100−4156, IRAS 00188−0856 and UGC 5101), all of which also display strong aromatic emission longwards of 6 μm. At shorter wavelengths, the observed flux density is unduly intense to share a common origin with the PAH features: this can be easily inferred by considering the shape of our SB template. If such emission is to be interpreted as the AGN-related hot dust continuum, one is in the presence of really contrasting signatures, since the aromatic nature of both the 6.2 and 7.7 μm peaks is beyond dispute. Conversely, in cases like the *blue* spectrum (IRAS 01298−0744) on the top of Fig. 9, the possibility that the tentative 6.2 μm feature is actually a ridge in the absorbed continuum mimicking the PAH emission cannot be ruled out. Moreover, the supposed 7.7 μm companion appears to be broad and roundish, as usually observed in the AGN-dominated spectra (as also the *green* ones, i.e. IRAS 16156+0146 and IRAS 08572+3915): this is rather a narrow window of unabsorbed continuum that immediately declines into the silicate trough. A possible explanation to the *anomalous* spectra can be the coexistence of a buried AGN component of moderate luminosity with a powerful SB. In this scenario, the direct AGN emission is quenched by a dense screen, producing deep absorption bands whose carriers are unknown (perhaps various ices and HAC, see above). The sharp disappearance of the hot dust continuum is justified if the blending reaches up to the 9.7 μm silicate feature. A hint in this direction is provided by the comparison between the contiguous spectra of IRAS 21219−1757 (*red*, unabsorbed) and IRAS 12127−1412 (*blue*): both these sources can be considered as pure AGN at 5–8 μm. In the former, we observe a featureless and uniform continuum, which is a reasonable candidate to outline the true hot dust emission of the latter source as well. In this case, however, the measured 8 μm flux density is well below that expected from the extrapolation of the putative continuum slope. Hence, it possibly represents only a saddle point between the broad ∼7 and 9.7 μm absorption bands.

The qualitative considerations above are of course insufficient to claim that very unusual physical conditions are responsible for the emergence of *anomalous* spectral shapes and absorption/reddening polarities. In order to properly investigate these aspects and characterize the *anomalous* sources, a detailed analysis is needed from *K* band up to ∼20 μm. This would make it possible to address the problems connected to the uncertain location of the continuum. For a few of our targets, this spectral range is nearly covered in its entirety, and interesting indications come from *L*- and *M*-band studies in which strong aliphatic and CO absorption features are detected: the red wing of the 4.65 μm CO profile is indeed entering the very beginning of the *Spitzer*–IRS window in several absorbed objects of our sample. None the less, a joint modelling of the 2–20 μm SED is at present frustrated by the disparity in signal-to-noise ratio and the scatter in flux calibration among the different ground-based and space facilities involved in the observations.

Summarizing, there seems to be no clear correlation between the degree of continuum reddening and the optical depth of individual absorption features. From a quantitative point of view, this has already been established by Sani et al. (2008) in an extensive *L*- and *M*-band study of five bright ULIRGs. The presence of *anomalous* sources in our sample challenges even the possibility of a stepwise correlation, which is instead found shortwards of 5 μm: neither the detection of broad absorption features implies invariably a sizable reddening nor a flat continuum is regularly unabsorbed. This should

not be surprising, since ULIRGs have a very disturbed morphology and large variations in chemical composition and geometrical structure of the dust are naturally expected. Yet it is possible to reconcile the observation of significant absorption features alongside apparent lack of reddening without invoking special dust distributions and covering factors. In Fig. 10, the optical depths of the main absorption features are plotted against the optical depth to the hot dust continuum. All these values are also included in Table 3. By focus-
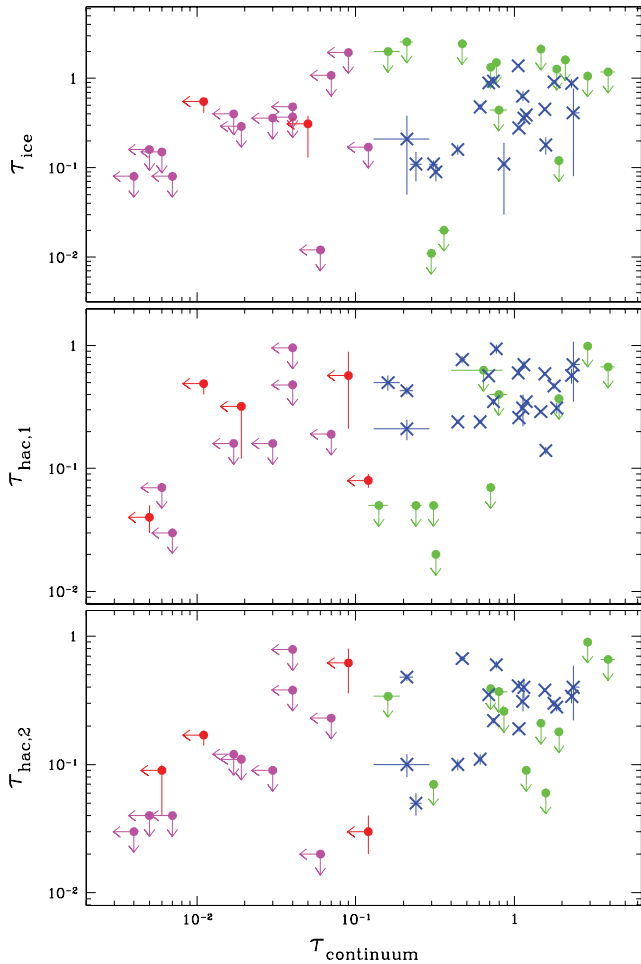
Figure 10. Opacity of absorption features versus continuum opacity, inferred from the reddening of the AGN component. From top to bottom panels, the three panels show the qualitative correlation between the optical depth of the main observed features (ascribed to water ice at ∼6.0 μm and HAC at ∼6.85 and ∼7.25 μm) and the optical depth to the hot dust continuum. In each plot, the blue crosses refer to well-established measurements of both quantities, while the other points render in a different colour code all the cases involving upper limits. Only the 50 AGN detections are considered, since no absorption is found in pure SBs. In a few cases, the observed AGN component is too faint and no sort of indication can be evinced about additional features: for this reason, the number of effective entries is 48, 43 and 43, respectively. The values of the optical depth for the three *anomalous* sources are computed assuming a flat AGN intrinsic continuum and a quasi-grey extinction law (see the discussion in the text) and are provided as upper limits on the vertical axis, since the identification of the single features is unclear. If we take into account the secure entries only, we evince that no strict proportionality holds between reddening and absorption, nevertheless they positively correlate. This evidence is not controverted by the other points, whose constraints are very limited. We conclude that the appearance of broad absorption coupled with reddening deficit is confidentially due to a flat extinction law.

ing on the confident entries only, the positive correlation between absorption and reddening is tentatively recovered. This suggests that modifications of the extinction law are possibly involved.

8.5 The extinction law

Conforming to our interpretation, both reddening and deep absorption are related to the presence of a compact power source, and must be almost exclusively due to cold material in the surroundings of the AGN component. We therefore argue that a reddened continuum is not observed in the *anomalous* sources because the actual extinction law applicable to their AGN component has a softer wavelength dependence. Within the power-law prescription $\tau_\lambda \propto \lambda^{-1.75}$ that has been adopted after Draine (1989), the ratio between the values of the optical depth at the red and blue ends of our fitting region is $\tau_{red}/\tau_{blue} \simeq 0.44$; this allows us to reproduce the steepest continuum gradients. Yet, according to the observations, the extinction curve can be safely described by a power law only up to ∼4–5 μm, and becomes rather controversial in the 5–8 μm range. For a long time, in absence of an adequate coverage of this spectral region with scientific data, the near-IR power-law trend was supposed to hold up to the 9.7 μm silicate bump. Only in the last decade, in the wake of the observations towards the Galactic Centre (Lutz et al. 1996), evidence has grown that the extinction curve can also undergo a flattening longwards of ∼4 μm, without giving rise to a clear minimum before the silicate feature (e.g. Indebetouw et al. 2005; Nishiyama et al. 2009 and references therein). Since we are applying extinction to a compact nuclear source, this flat variant represents another reasonable choice. Moreover, all the *anomalous* sources (regardless of their absorption features) have a very steep *L*-band continuum, suggesting that the AGN component is actually reddened and that some change in the extinction pattern may occur at longer wavelengths.

In order to test this scenario, we have performed our AGN/SB decomposition once again, this time assuming the analytical form of Chiar & Tielens (2006) for the wavelength dependence of the optical depth. The intrinsic slope of the AGN template remains $\Gamma_{AGN} = 1.5$. The alternate extinction law is really quasi-grey in our working range, since $\tau_{red}/\tau_{blue} \simeq 0.90$ (and $\tau_{red}/\tau_6 \simeq 0.96$). This entails a degeneracy between the AGN flux amplitude and its optical depth, in spite of which we are able to reach important conclusions. The overall results can be summarized in terms of subclasses. (a) A flat extinction can be safely ruled out for eight sources, whose observed continuum is too steep to be reproduced within the new framework. This group encompasses all the objects with $\alpha_{bol} > 0.25$ and $\tau_6 > 1$ according to the previous estimate; the only exception is IRAS 15250+3609. (b) The objects whose classification is unchanged reach up to 30, by combining 19 out of 21 pure SBs (save IRAS 02411+0353 and IRAS 16487+5447 that may contain a faint AGN component) and 11 out of 14 composite sources hosting a non-extinguished AGN. (c) The remaining three, along with IRAS 07598+6508, IRAS 19254−7245, the above-mentioned IRAS 16487+5447 and other four mildly reddened sources, have a non-degenerate fitting output. (d) Finally, there are 23 objects (including the *anomalous* ones) that can be fitted with the modified extinction but are affected by the normalization/absorption degeneracy. It has been possible to remove such degeneracy in 20 cases, by pegging the value of the optical depth after our previous *L*-band studies.

The consequence of a quasi-grey extinction has been tested by computing the new values of *R* and α_6 and checking their rearrangement with respect to the former best fit of the *R*–α_6 relation.
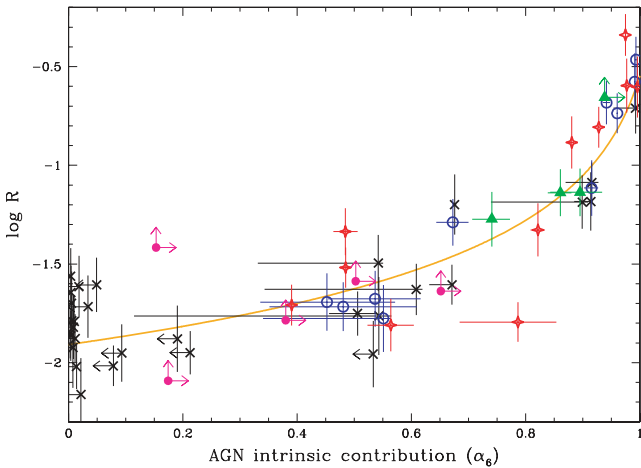
Figure 11. R–α_6 plot obtained by assuming a quasi-grey extinction law for the AGN component. The new positions of the sources are compared with those obtained with a power-law extinction: the orange solid line is indeed the best fit of the R–α_6 relation from equation (4). Different colours and symbols are used according to the following: black crosses for sources confirmed to host a non-extinguished AGN component, if any; blue rings for sources with a definite fit in the new scenario; red diamonds for sources whose normalization has been fixed through their L-band spectra; green triangles for sources in which the removal of the normalization/absorption degeneracy is tentative, due to the lower quality of the L-band spectra; magenta points for sources appearing as pure SBs in the L band.

The outcome is shown in Fig. 11, and implies two interesting results: (1) a flat extinction law seems suitable to describe the dusty environment surrounding the AGN component in many ULIRGs and (2) in a statistical sense, the assumption of a quasi-grey extinction does not alter our global results, once the optical depth is reliably estimated through additional constraints. In conclusion, the large size and the spectral variety of our sample suggest that the AGN component inside a ULIRG cannot be described in terms of a universal 5–8 μm extinction pattern: both a power-law and a soft wavelength dependence of the optical depth appear to be involved. In addition to a different dust amount and composition along the line of sight, this is possibly also due to geometrical effects, such as the orientation of the obscuring torus itself and/or the clumpiness of the circumnuclear star-forming cores. It is however important to keep in mind the limitations of our approach: our description does not take into account the possible effects of radiative transfer that can be essential even at 5–8 μm. In particular, the deviations from a power-law extinction could be related to a lesser accuracy of the screen approximation, which is instead correct for the Galactic Centre. This issue represents a critical challenge for any future study of the dust properties and near- and mid-IR extinction in AGN and ULIRGs.

8.6 Trend with bolometric luminosity

Once the relative AGN/SB fraction of ULIRG luminosity has been estimated, one of the main issues to investigate is the possibility of a larger AGN contribution at higher luminosities. Interestingly, no clear trend in the detection of [Ne v] $\lambda14.32$ as a function of the total IR luminosity has been discovered by Farrah et al. (2007). This is in contrast with several studies based on optical spectroscopy, which instead suggest the existence of a growing trend. This claim finds the first convincing confirmation with the *histograms* of Veilleux et al. (1999a), indicating that AGN-like systems (i.e. those classified as

Seyferts, without considering the possible integration of LINERs) represent only a small percentage among IR galaxies below $L_{IR} < 10^{11}$ L$_\odot$, but increase to become the most populated subset in the luminosity range $10^{12.3} < L_{IR} < 10^{12.8}$ L$_\odot$. Moreover, virtually all the hyperluminous IR galaxies (HLIRGs; $L_{IR} > 10^{13}$ L$_\odot$) seem to harbour a powerful AGN, at least up to $z \lesssim 1$ (Rowan-Robinson 2000). The key point is that such a result still has to be read in terms of AGN detectability, and not necessarily of larger AGN contribution. In a skeptical perspective, even this detectability trend could be contrived by selection effects: as we have already pointed out, a considerable amount of sources that are optically classified as H II regions actually harbours obscured but non-negligible AGN components. Furthermore, a general consensus has grown in the last years about the sharp decrease in the fraction of absorbed AGN with X-ray luminosity (Ueda et al. 2003; Hasinger 2008). At mid-IR wavelengths, a clear AGN preponderance at high luminosity is found by Tran et al. (2001), with SBs and AGN dominating the energy output, respectively, at the lower and higher ends of the ULIRG range. It is then worthwhile checking how our results fit into this question, even though our coverage of bolometric luminosity is limited.

Assuming the standard divide of $\log(L_{IR}/L_\odot) = 12.3$, the population of the two subsets consisting of the sources whose luminosity is below and above this threshold is 55 and 16, respectively. We recall that simply by solving the ambiguity concerning LINERs we are able to detect a much larger number of AGN (50 out of 71 ULIRGs) with respect to optical studies. The positive detections involve ∼2/3 of the *faint* sources and ∼3/4 of the *bright* ones. Such fractions are too similar to hint at a clear increase. Nevertheless, by computing the AGN contribution α_{AGN} to both bins of luminosity we obtain two well-separated values:

$$\alpha_{AGN} = \frac{\sum \alpha_i L_i}{\sum L_i} = \begin{cases} 18.2^{+0.6}_{-1.0} & [\log(L_{IR}/L_\odot) < 12.3] \\ 30.9^{+1.4}_{-1.3} & [\log(L_{IR}/L_\odot) > 12.3] \end{cases},$$

where α and L stand for the previous α_{bol} and L_{IR}. This is robust evidence in favour of the growing trend with bolometric luminosity of the AGN content inside ULIRGs.[8] An illustration of this effect, that will be addressed in detail in a forthcoming paper (Nardini et al., in preparation) by enlarging the statistics at the highest luminosities (see also Imanishi 2009), is provided in Fig. 12.

In conclusion, considering only the 63 sources from the 1 Jy sample, AGN are responsible for $23.1^{+0.7}_{-0.9}$ per cent of the ULIRG luminosity in the local Universe. We underline that this estimate is not biased due to selection effects. Concerning the seven missing sources which undermine the sample completeness, by simply assuming the average properties of their optical class for the five type 2 Seyferts (i.e. $\alpha_{bol} \simeq 0.29$) and an SB-dominated nature for the two unclassified objects we are able to confirm the value provided above. Only in the extreme case of null AGN significance for all the seven sources, the global contribution of accretion processes to IR activity should be reduced by ∼2 per cent. The same amplitude in the opposite direction is predicted after correcting for a possible bias towards star formation, connected to the *cold* 60 μm selection.

---

[8] There is indeed a difference in the cosmological parameters between this work and that of Kim & Sanders (1998), on which the mentioned investigations of the 1 Jy sample at optical wavelengths are based. This slightly affects the estimate of the bolometric luminosities, with an upward shift of ∼0.1 dex at the highest luminosity distances: about 10 sources enter the higher luminosity bin. We have taken into account this effect, and found that the trend is both qualitatively and quantitatively confirmed.
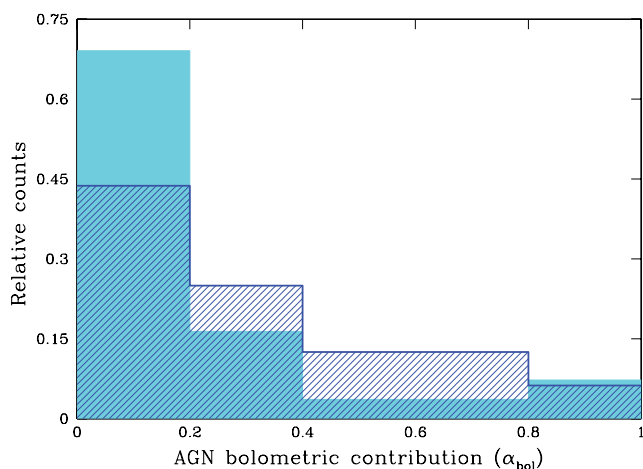
Figure 12. Relative number counts within the different bins of AGN contribution. The two distributions correspond to the populations of sources with $\log(L_{IR}/L_{\odot}) < 12.3$ (cyan) and $\log(L_{IR}/L_{\odot}) > 12.3$ (shaded blue).

Not even the inclusion of the eight southern ULIRGs in the computation affects our results, since they form a complete and fully representative subset.

The recent and comprehensive work of Veilleux et al. (2009) investigates with great detail the connection between local ULIRGs and PG quasars; the contribution of nuclear activity to the bolometric luminosity of ULIRGs is obtained by means of six independent methods based on the *Spitzer*–IRS spectra. Fine-structure line ratios, aromatic features and continuum colours have been employed: a comparison among the six different estimates provided for the single sources gives a good idea of the uncertainties involved that sometimes can be pretty large. The ensemble average hints at a slightly higher AGN contribution (∼35–40 per cent) with respect to the findings of our study and the previous literature. This could be due to a possible bias in Veilleux et al. (2009), related to the choice of PG quasars as *zero-points* for the nuclear activity within ULIRGs. However, by simply restricting to the 48 common sources, our estimate increases to ∼30 per cent as well, and the results are definitely in good agreement.

9 CONCLUSIONS

In this paper, we have presented a 5–8 μm spectral study of a large and representative sample of local ULIRGs, based on *Spitzer*–IRS observations. We have explored the role of black hole accretion and vigorous star formation as the power source of the extreme IR activity, assessing the gravitational and stellar origin of ULIRG emission by modelling their 5–8 μm spectra through a couple of AGN and SB templates. In this wavelength range, in fact, the spectral properties of AGN and SBs are widely different, and only moderate dispersion is found within each class. It is then possible to accomplish a sharp characterization of both the AGN and SB components, and disentangle their contribution to the observed emission. Our method has proven to be successful in unveiling intrinsically faint or heavily obscured AGN components, leading to a total of 50 convincing detections out of the 71 sources in our sample. Such a large AGN detection rate can be achieved only by resorting to the most effective multiwavelength diagnostics. As a consequence, AGN turn out to be very common among ULIRGs in the local Universe, even if they are usually not significant as contributors to the global energetics of the host galaxy when compared to the SBs.

A simple analytical model, in fact, also allows us to obtain a reliable estimate of the AGN/SB contribution to the overall energy output of each source. For the sake of a gross classification, we can define the following *one-third rule*: assuming a significance threshold of 1/3 in the AGN/SB bolometric contribution, i.e. $\alpha_{bol} = 0.25$, we find that one-third of ULIRGs harbour a sizable AGN, one-third harbour a negligible AGN and one-third harbour no AGN at all. Star formation is then confirmed as the dominant energy source underlying the ULIRG activity. In more quantitative terms, AGN account for ∼23 per cent of the global ULIRG emission, approaching and possibly exceeding ∼30 per cent at higher luminosities. This increasing trend is clearly brought out: the average AGN *weight* rises from 18 to 31 per cent above the luminosity threshold of $L_{IR} = 10^{12.3}$ L$_{\odot}$.

Thanks to the large size of our sample we have also been able to test the properties of the obscuring material, in particular of the extinction law applicable to the AGN-related hot dust continuum. Observations reveal a lack of correlation between the continuum reddening and the presence of deep absorption features, suggesting that the extinction of the AGN component in a ULIRG environment is not universal. Both a power-law and a quasi-grey behaviour of the optical depth as a function of wavelength are necessary to account for the emission of different objects and seem to be involved among ULIRGs. Large differences in the chemical composition and geometrical structure of the dust are supported by the spread in the intensity (and sometimes also the shape) of the most frequent absorption profiles. Although our method is not suitable to fully investigate these aspects, it is extremely powerful for global classification and can be applied whenever spectra of sufficient quality are available. Moreover, it can be turned into a photometric method to study fainter sources, using diagnostics such as the bolometric correction and the continuum slope, which can be measured efficiently with the upcoming IR facilities.

REFERENCES

Antonucci R., 1993, ARA&A, 31, 473
Antonucci R. R. J., Miller J. S., 1985, ApJ, 297, 621
Armus L. et al., 2006, ApJ, 640, 204
Armus L. et al., 2007, ApJ, 656, 148
Balestra I., Boller T., Gallo L., Lutz D., Hess S., 2005, A&A, 442, 469
Blain A. W., Smail I., Ivison R. J., Kneib J.-P., Frayer D. T., 2002, Phys. Rev., 369, 111
Boogert A. C. A. et al., 2008, ApJ, 678, 985
Braito V. et al., 2003, A&A, 398, 107
Braito V. et al., 2004, A&A, 420, 79
Braito V., Reeves J. N., Della Ceca R., Ptak A., Risaliti G., Yaqoob T., 2009, A&A, in press (arXiv:0905.1041)
Brandl B. R. et al., 2006, ApJ, 653, 1129 (B06)
Caputi K. I. et al., 2007, ApJ, 660, 97
Chiar J. E., Tielens A. G. G. M., 2006, ApJ, 637, 774

Chiar J. E., Tielens A. G. G. M., Whittet D. C. B., Schutte W. A., Boogert A. C. A., Lutz D., van Dishoeck E. F., Bernstein M. P., 2000, ApJ, 537, 749

Clements D. L., Sutherland W. J., McMahon R. G., Saunders W., 1996, MNRAS, 279, 477

Dartois E., Muñoz-Caro G. M., 2007, A&A, 476, 1235

Dasyra K. M. et al., 2006, ApJ, 638, 745

Downes D., Eckart A., 2007, A&A, 468, L57

Draine B. T., 1989, in Kaldeich B. H., ed., Proc. 22nd ESLAB Symp., Infrared Spectroscopy in Astronomy, ESA SP-290. ESA, Noordwijk, p. 93

Duc P.-A., Mirabel I. F., Maza J., 1997, A&AS, 124, 533

Dudik R. P., Satyapal S., Marcu D., 2009, ApJ, 691, 1501

Farrah D. et al., 2007, ApJ, 667, 149

Fisher K. B., Huchra J. P., Strauss M. A., Davis M., Yahil A., Schlegel D., 1995, ApJS, 100, 69

Förster Schreiber N. M., Roussel H., Sauvage M., Charmandaris V., 2004, A&A, 419, 501

Franceschini A. et al., 2003, MNRAS, 343, 1181

Gallagher S. C., Brandt W. N., Chartas G., Garmire G. P., Sambruna R. M., 2002, ApJ, 569, 655

Genzel R. et al., 1998, ApJ, 498, 579 (G98)

Gonzalez-Martin O., Masegosa J., Marquez I., Guainazzi M., Jimenez-Bailon E., 2009, A&A, in press (arXiv:0905.2973)

Hasinger G., 2008, A&A, 490, 905

Hinshaw G. et al., 2009, ApJS, 180, 225

Houck J. R., Schneider D. P., Danielson G. E., Neugebauer G., Soifer B. T., Beichman C. A., Lonsdale C. J., 1985, ApJ, 290, L5

Houck J. R. et al., 2004, ApJS, 154, 18

Imanishi M., 2009, ApJ, 694, 751

Imanishi M., Dudley C. C., 2000, ApJ, 545, 701

Imanishi M., Terashima Y., 2004, AJ, 127, 758

Imanishi M., Dudley C. C., Maloney P. R., 2001, ApJ, 558, L93

Imanishi M., Terashima Y., Anabuki N., Nakagawa T., 2003, ApJ, 596, L167

Imanishi M., Dudley C. C., Maloney P. R., 2006, ApJ, 637, 114

Imanishi M., Dudley C. C., Maiolino R., Maloney P. R., Nakagawa T., Risaliti G., 2007, ApJS, 171, 72

Indebetouw R. et al., 2005, ApJ, 619, 931

Iwasawa K., Sanders D. B., Evans A. S., Trentham N., Miniutti G., Spoon H. W. W., 2005, MNRAS, 357, 565

Keane J. V., Tielens A. G. G. M., Boogert A. C. A., Schutte W. A., Whittet D. C. B., 2001, A&A, 376, 254

Kessler M. F. et al., 1996, A&A, 315, L27

Kim D.-C., Sanders D. B., 1998, ApJS, 119, 41

Komossa S., Burwitz V., Hasinger G., Predehl P., Kaastra J. S., Ikebe Y., 2003, ApJ, 582, L15

Laurent O., Mirabel I. F., Charmandaris V., Gallais P., Madden S. C., Sauvage M., Vigroux L., Cesarsky C., 2000, A&A, 359, 887

Lutz D. et al., 1996, A&A, 315, L269

Lutz D., Veilleux S., Genzel R., 1999, ApJ, 517, L13

Lutz D. et al., 2007, ApJ, 661, L25

Lutz D. et al., 2008, ApJ, 684, 853

Maiolino R. et al., 2003, MNRAS, 344, L59

Maiolino R., Shemmer O., Imanishi M., Netzer H., Oliva E., Lutz D., Sturm E., 2007, A&A, 468, 979

Moorwood A. F. M., 1986, A&A, 166, 4

Nagar N. M., Wilson A. S., Falcke H., Veilleux S., Maiolino R., 2003, A&A, 409, 115

Nandra K., Iwasawa K., 2007, MNRAS, 382, L1

Nardini E., Risaliti G., Salvati M., Sani E., Imanishi M., Marconi A., Maiolino R., 2008, MNRAS, 385, L130 (Paper I)

Netzer H. et al., 2007, ApJ, 666, 806 (N07)

Nishiyama S., Nagata T., Tamura M., Kandori R., Hatano H., Sato S., Sugitani K., 2008, ApJ, 680, 1174

Nishiyama S., Tamura M., Hatano H., Kato D., Tanabé T., Sugitani K., Nagata T., 2009, ApJ, 696, 1407

Oyabu S., Kawara K., Tsuzuki Y., Matsuoka Y., Sameshima H., Asami N., Ohyama Y., 2009, ApJ, 697, 452

Peeters E., Spoon H. W. W., Tielens A. G. G. M., 2004, ApJ, 613, 986

Pernechele C., Berta S., Marconi A., Bonoli C., Bressan A., Franceschini A., Fritz J., Giro E., 2003, MNRAS, 338, L13

Persic M., Rephaeli Y., 2002, A&A, 382, 843

Ptak A., Heckman T., Levenson N. A., Weaver K., Strickland D., 2003, ApJ, 592, 782

Reynolds C. S., Nowak M. A., 2003, Phys. Rev., 377, 389

Rigopoulou D., Spoon H. W. W., Genzel R., Lutz D., Moorwood A. F. M., Tran Q. D., 1999, AJ, 118, 2625

Risaliti G., Gilli R., Maiolino R., Salvati M., 2000, A&A, 357, 13

Risaliti G. et al., 2003, ApJ, 595, L17

Risaliti G. et al., 2006a, ApJ, 637, L17

Risaliti G. et al., 2006b, MNRAS, 365, 303

Rowan-Robinson M., 2000, MNRAS, 316, 885

Sakamoto K. et al., 2008, ApJ, 684, 957

Sanders D. B., Mirabel I. F., 1996, ARA&A, 34, 749

Sanders D. B., Soifer B. T., Elias J. H., Neugebauer G., Matthews K., 1988, ApJ, 328, L35

Sanders D. B., Mazzarella J. M., Kim D.-C., Surace J. A., Soifer B. T., 2003, AJ, 126, 1607

Sani E. et al., 2008, ApJ, 675, 96

Schweitzer M. et al., 2006, ApJ, 649, 79

Scoville N. Z. et al., 2000, AJ, 119, 991

Severgnini P., Risaliti G., Marconi A., Maiolino R., Salvati M., 2001, A&A, 368, 44

Soifer B. T., Neugebauer G., 1991, AJ, 101, 354

Soifer B. T., Neugebauer G., Matthews K., Becklin E. E., Ressler M., Werner M. W., Weinberger A. J., Egami E., 1999, ApJ, 513, 207

Spoon H. W. W. et al., 2004, ApJS, 154, 184

Spoon H. W. W., Marshall J. A., Houck J. R., Elitzur M., Hao L., Armus L., Brandl B. R., Charmandaris V., 2007, ApJ, 654, L49

Strauss M. A., Huchra J. P., Davis M., Yahil A., Fisher K. B., Tonry J., 1992, ApJS, 83, 29

Taniguchi Y., Yoshino A., Ohyama Y., Nishiura S., 1999, ApJ, 514, 660

Teng S. H., Wilson A. S., Veilleux S., Young A. J., Sanders D. B., Nagar N. M., 2005, ApJ, 633, 664

Teng S. H., Veilleux S., Wilson A. S., Young A. J., Sanders D. B., Nagar N. M., 2008, ApJ, 674, 133

Tran Q. D. et al., 2001, ApJ, 552, 527

Ueda Y., Akiyama M., Ohta K., Miyaji T., 2003, ApJ, 598, 886

Veilleux S., Osterbrock D. E., 1987, ApJS, 63, 295

Veilleux S., Kim D.-C., Sanders D. B., Mazzarella J. M., Soifer B. T., 1995, ApJS, 98, 171

Veilleux S., Kim D.-C., Sanders D. B., 1999a, ApJ, 522, 113

Veilleux S., Sanders D. B., Kim D.-C., 1999b, ApJ, 522, 139

Veilleux S., Kim D.-C., Sanders D. B., 2002, ApJS, 143, 315

Veilleux S. et al., 2009, ApJS, 182, 628

Vignati P. et al., 1999, A&A, 349, L57

Voit G. M., 1992, MNRAS, 258, 841

Werner M. W. et al., 2004, ApJS, 154, 1

APPENDIX A: ADDITIONAL NOTES AND SPECTRAL FITS

With the exception of IRAS 08559+1053, that was observed in the early stage of the mission (before the start of the regular scientific operations) and is analysed for the first time in the present work, the low- and/or high-resolution *Spitzer*–IRS spectra of the sources in our sample have already been shown and widely discussed by Armus et al. (2007), Farrah et al. (2007), Imanishi et al. (2007) and Veilleux et al. (2009). In the following, we add some additional comments about a few interesting objects, and show the full results of our spectral decomposition (Fig. A1).

A1 The nature of ARP 220

In spite of being the nearest (at ∼80 Mpc) and best-studied ULIRG, ARP 220 is still puzzling and controversial with respect to its
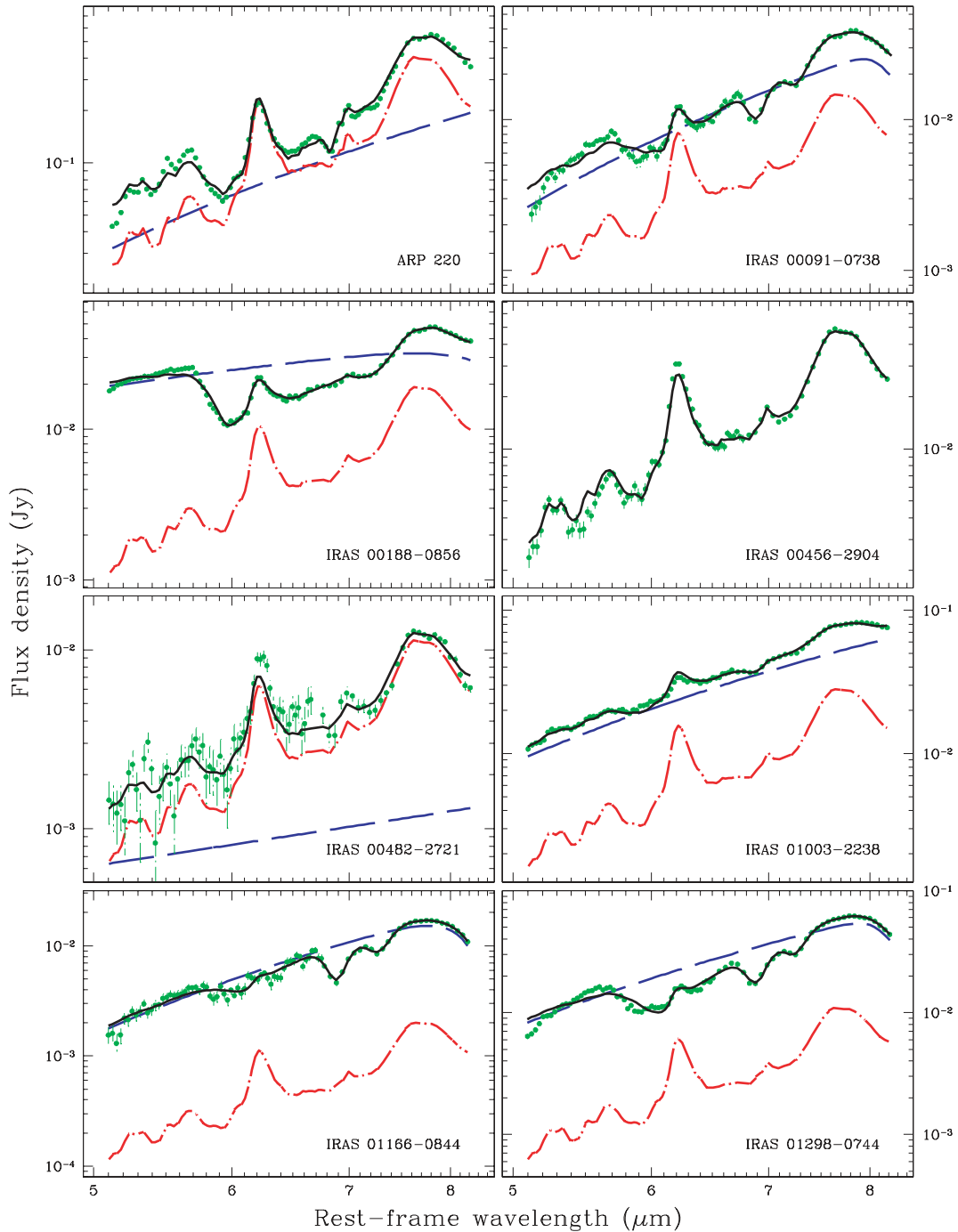
Figure A1. Best fits and spectral components.

energy source. The multiwavelength SED of this interacting system has been often employed as a template to constrain the emission of star-forming galaxies at high redshift, but the pure SB scenario is actually challenged by many independent pieces of observational evidence, and the alleged action of an extremely obscured and elusive black hole in the western nucleus is widely debated. Such a possibility is strengthened by recent interferometric observations, outlining a compact and massive ring of hot dust that straightly recalls the toroidal structures around AGN (Downes & Eckart 2007 and references therein for additional hints to the presence of an AGN inside ARP 220). It is somewhat arbitrary to assess the intrinsic lu-

minosity of this core; the western nucleus is anyway the brightest one by a factor of ∼3 (Soifer et al. 1999) and the AGN component, if confirmed, would be absolutely relevant. Our diagnostic method discloses a contribution to the bolometric luminosity of the whole system arising from a highly obscured AGN that reaches up to 20 per cent. This value should be read with some caution, also due to the peculiar properties of the aromatic emission in ARP 220 (e.g. the suppression of the 6.2 μm feature with respect to the 7.7 μm one) that may alter the continuum decomposition based on AGN/SB templates; yet it represents a stirring indication of magnitude. The matter is fully open, and further incentive is provided by
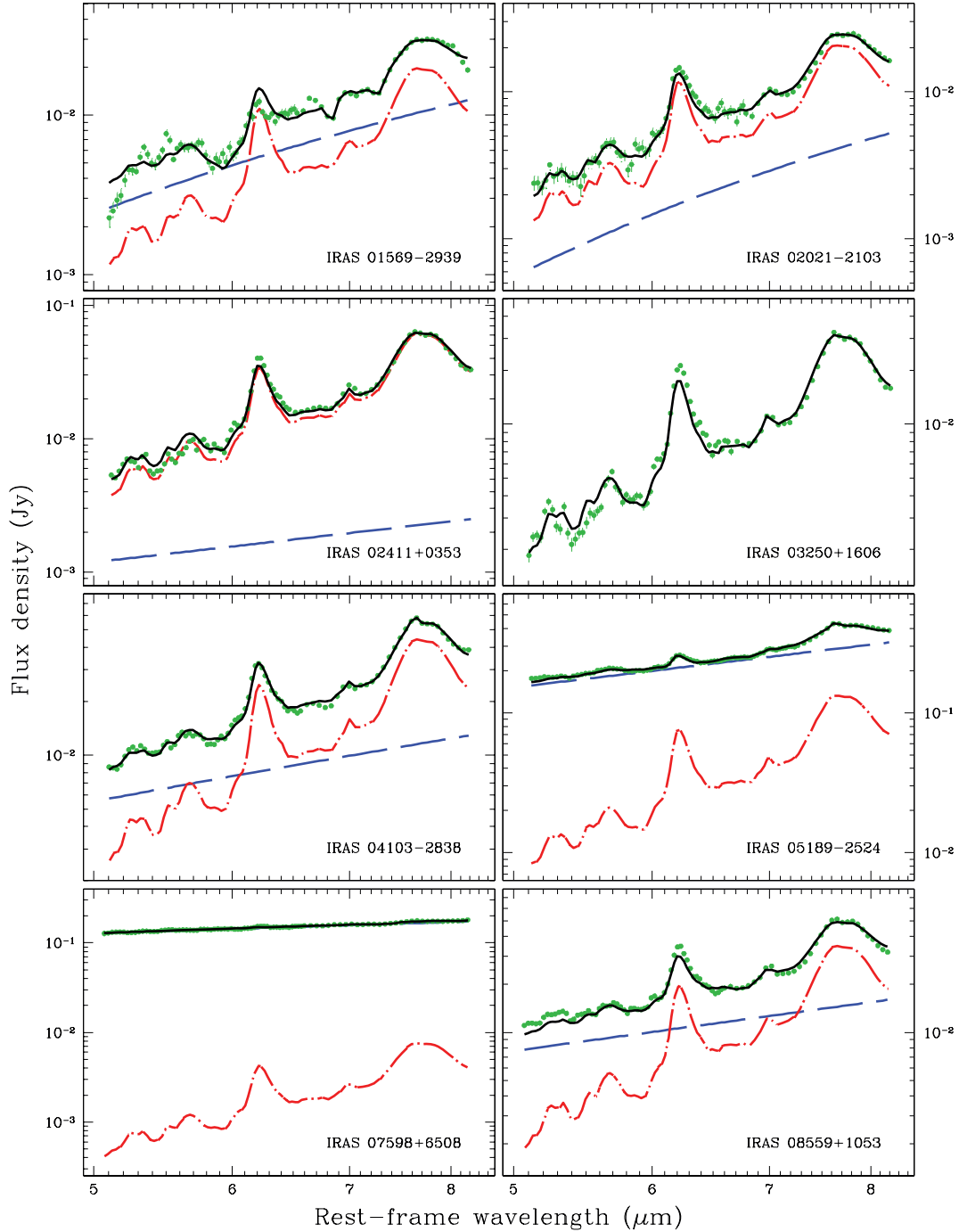
Figure A1 – *continued*

Sakamoto et al. (2008), whose precise discussion about the nature of the compact luminous source located in the western nucleus, in terms of both an AGN and a collection of overlapping super star clusters, makes the latter explanation appear as slightly strained.

A2 The iron Kα line in IRAS 04103−2838

IRAS 04103−2838 is optically classified as a LINER and is a *warm* ULIRG according to its IRAS colours ($f_{25}/f_{60} = 0.30$). We are able to unveil an AGN component at 5–8 μm, whose contribution to the bolometric luminosity is estimated as ∼6 per cent. The presence

of an AGN is confirmed by the detection of a broad Kα line at ∼6.4 keV, during a recent *XMM–Newton* observation (Teng et al. 2008). Due to the large equivalent width (∼1.65 keV) of this iron feature, the AGN is supposed to be Compton-thick, anyway it does not seem to dominate the total energy output of the source.

A3 The 7.65 μm fine-structure line

IRAS 17179+5444 exhibits a prominent emission at ∼7.65 μm, blended with the adjacent PAH feature, that we interpret as the unresolved [Ne vi] fine-structure line. Due to its ionization energy of
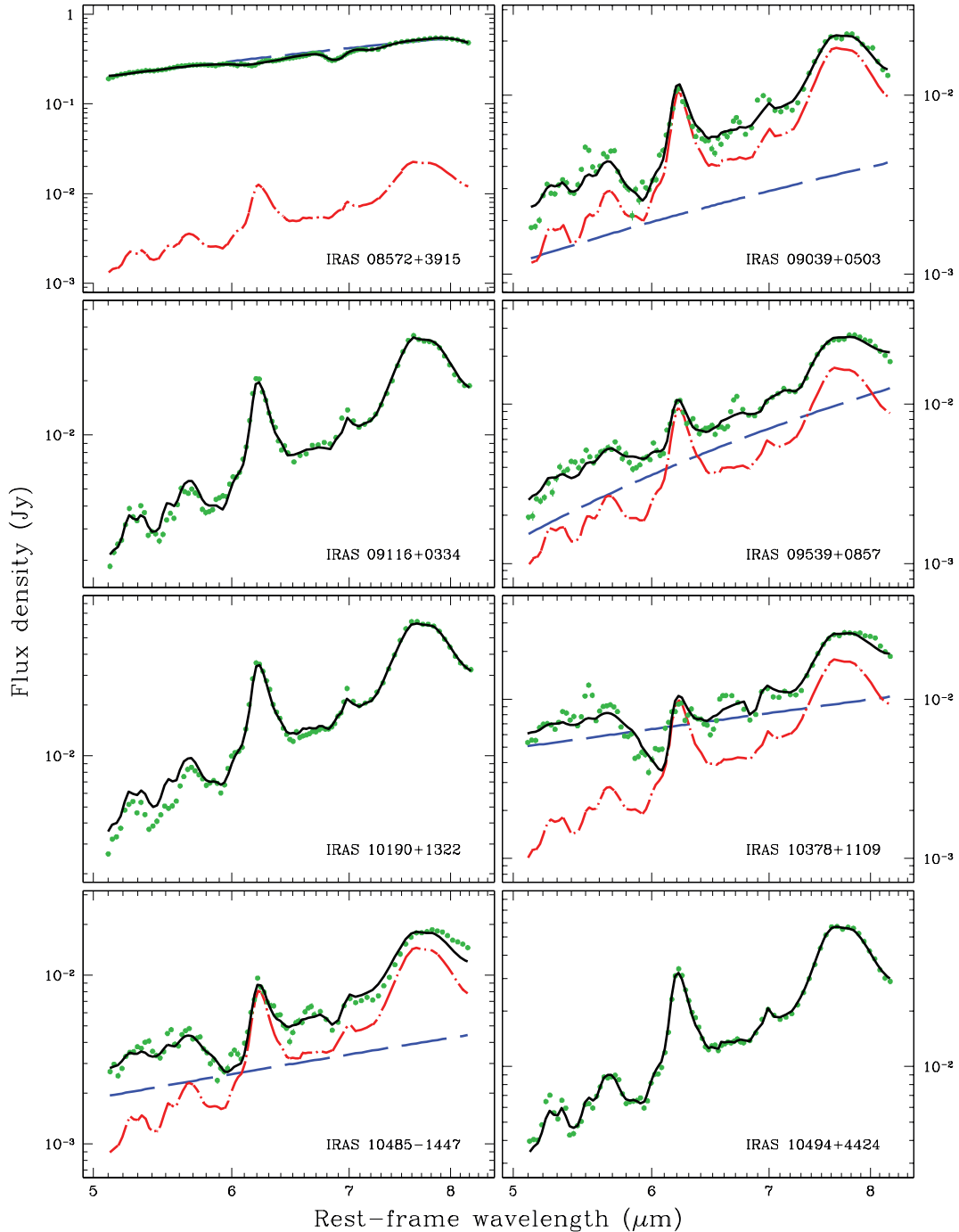
Figure A1 – *continued*

126 eV, this feature is connected to the hardest nuclear activity, and indeed it is convincingly observed also in other three Seyfert galaxies (IRAS 05189−2524, IRAS 12072−0444 and IRAS 13454−2956) plus IRAS 04103−2838. Fluxes and equivalent widths are listed in Table A1, and are in good agreement with the values provided by Veilleux et al. (2009) for their positive detections. We note that our identification of this line also in IRAS 04103−2838 represents the first detection involving a non-Seyfert ULIRG. In IRAS 17179+5444, the strength of [Ne vi] is anomalously high, as evinced through both a visual inspection and a com-

parison with the [Ne v] lines at longer wavelengths (Farrah et al. 2007). This is a very interesting case, since after a separate check of the single spectra from each nod position the line is confirmed to be genuine.

A4 The case study of NGC 6240

As mentioned, many X-ray observations suggest the possible presence in NGC 6240 of a pair of supermassive black holes hidden behind large column densities of screening material. A
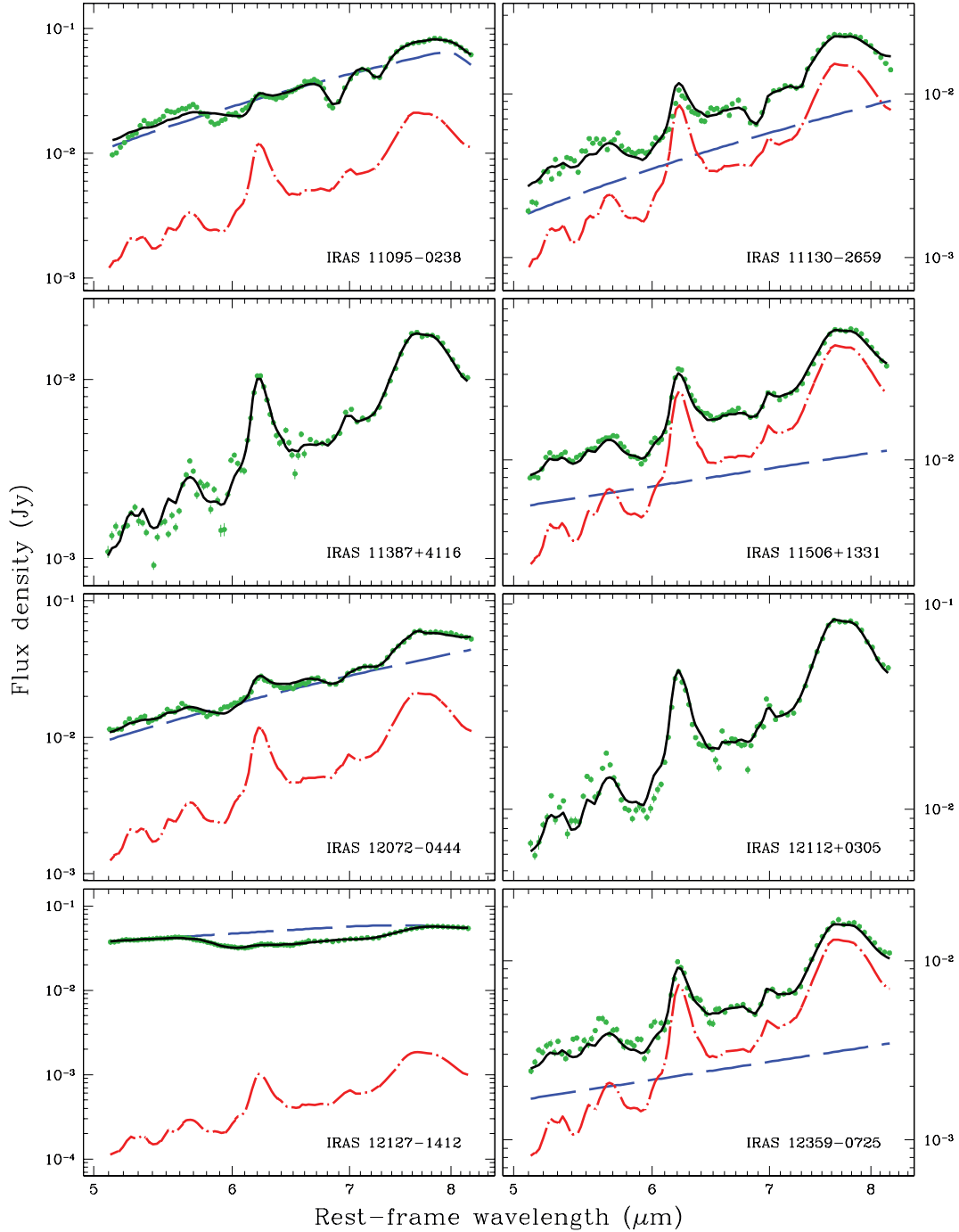
Figure A1 – *continued*

detailed IR study pivoted on the *Spitzer*–IRS spectrum and integrated with photometric data from near- to far-IR is presented by Armus et al. (2006). As a result of the SED modelling, a hot dust component at ∼700 K is found, accounting for ∼3.5 per cent of the bolometric luminosity and pointing to the presence of a buried AGN. The AGN contribution is again estimated as ∼3–5 per cent through high-ionization lines, but can raise up to ∼20–24 per cent if correcting the [Ne v]/[Ne ii] ratio for the extinction derived from the hard X-ray data. Our estimate of α_{bol} (4.5–11.5 per cent) is then fully reliable, in spite of the great simplicity of our method as opposed to a multicomponent fit of the whole IR

SED, which is anyway necessary to fully characterize an individual source.

A5 Spectral fits

The panels of Fig. A1 illustrate the results of our AGN/SB decomposition at 5–8 μm. Along with the data points (green filled circles) and the best-fitting model (black solid line), both contributions are plotted: the SB component (red dot–dashed line) and the observed AGN continuum (blue long-dashed line).
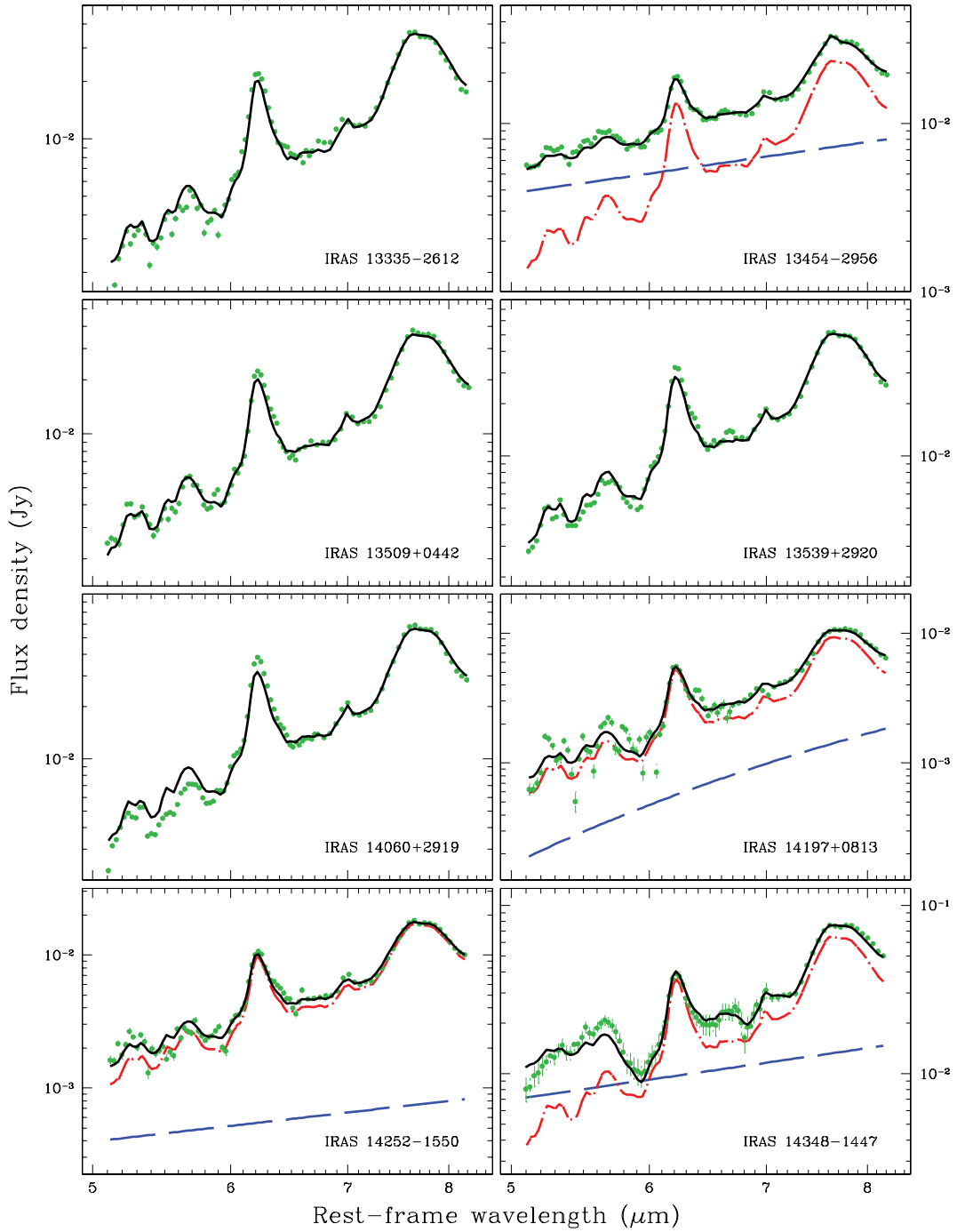
Figure A1 – *continued*
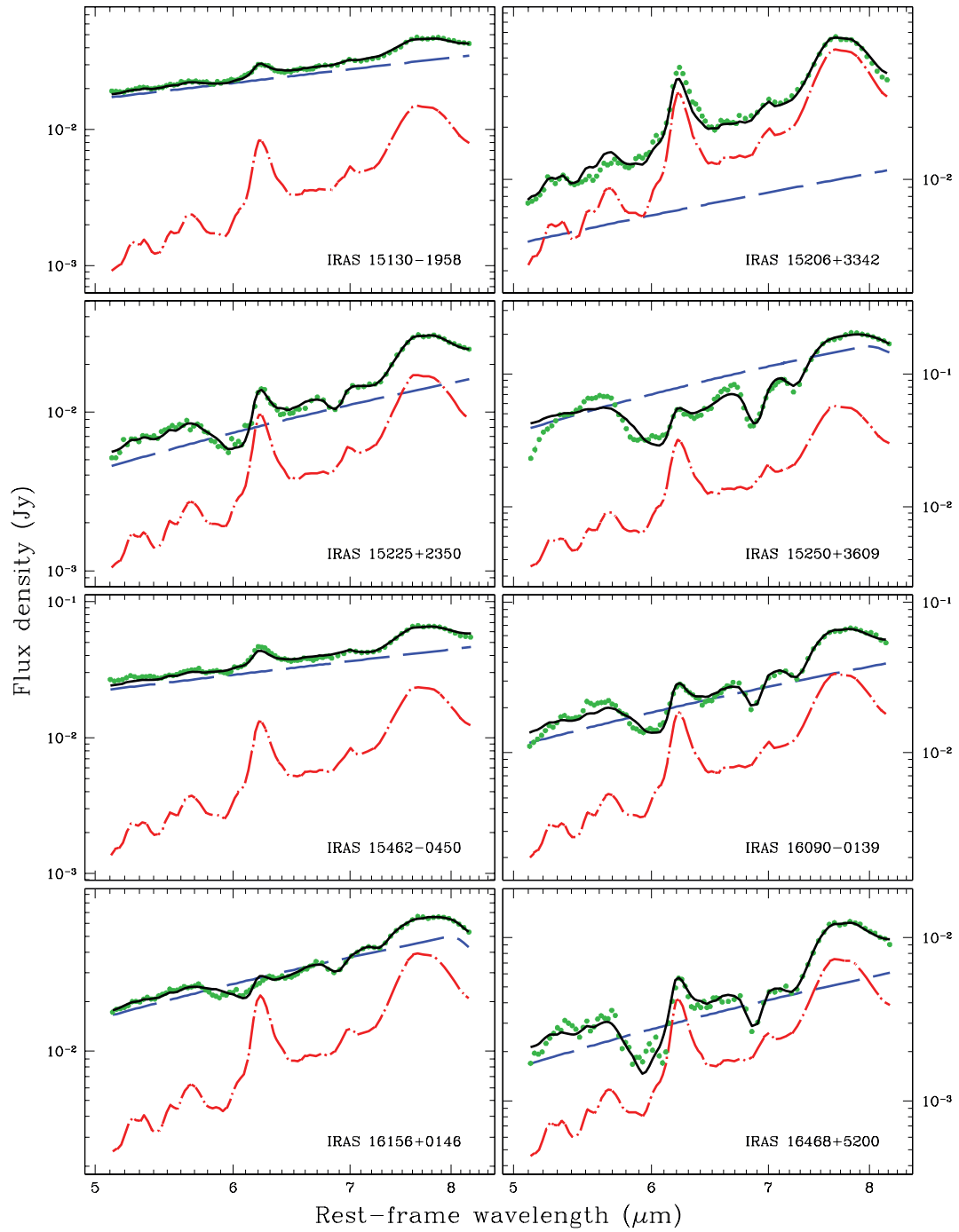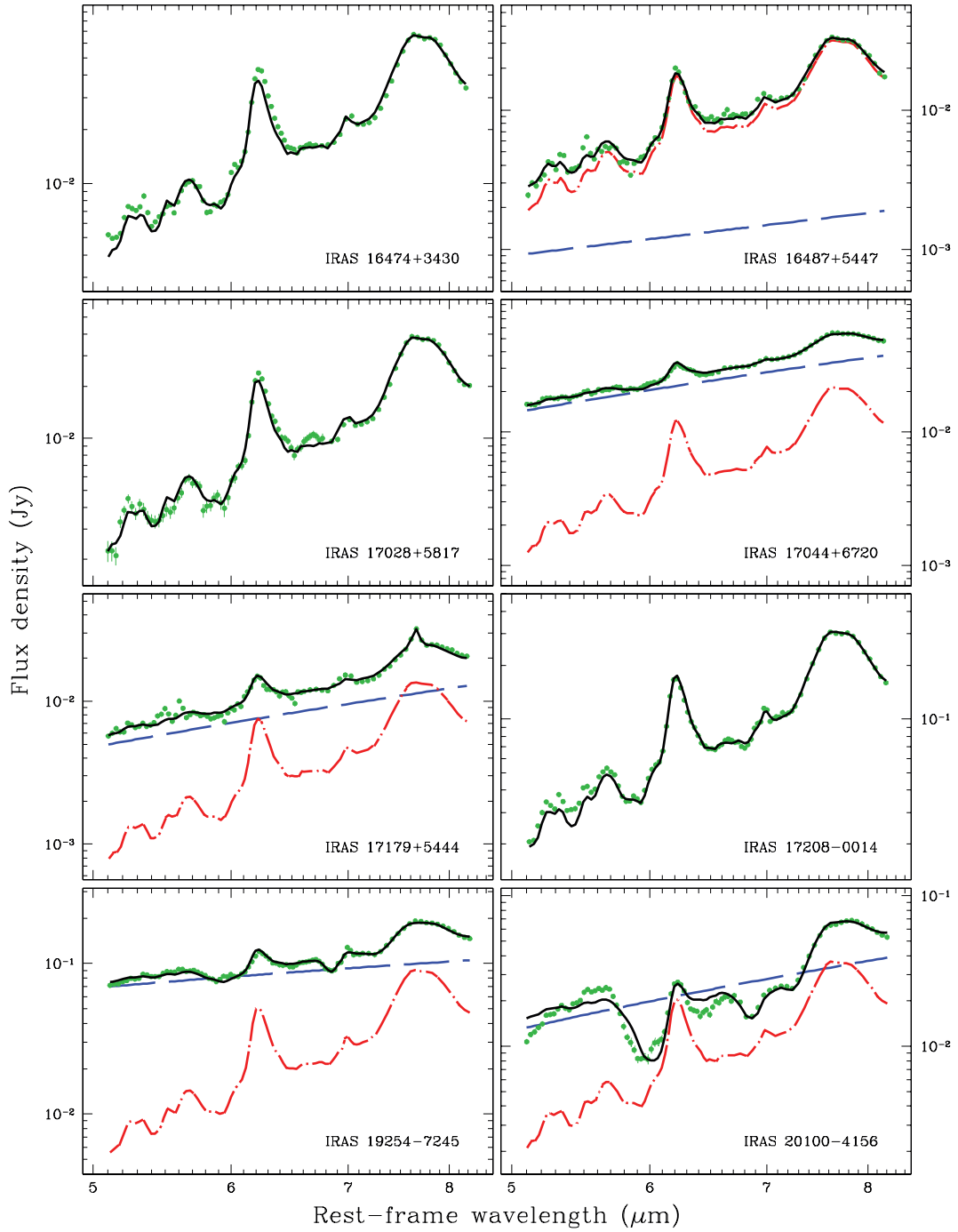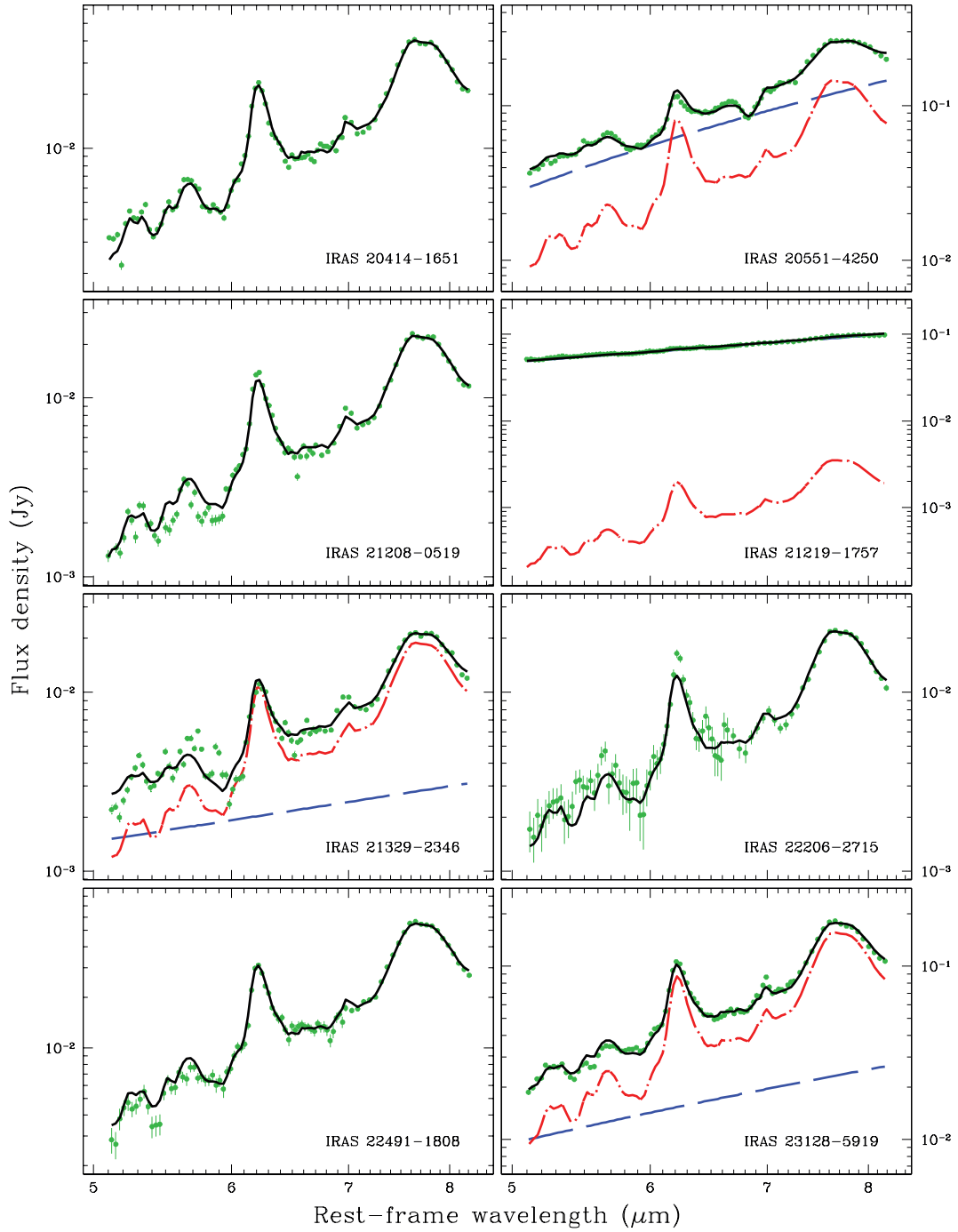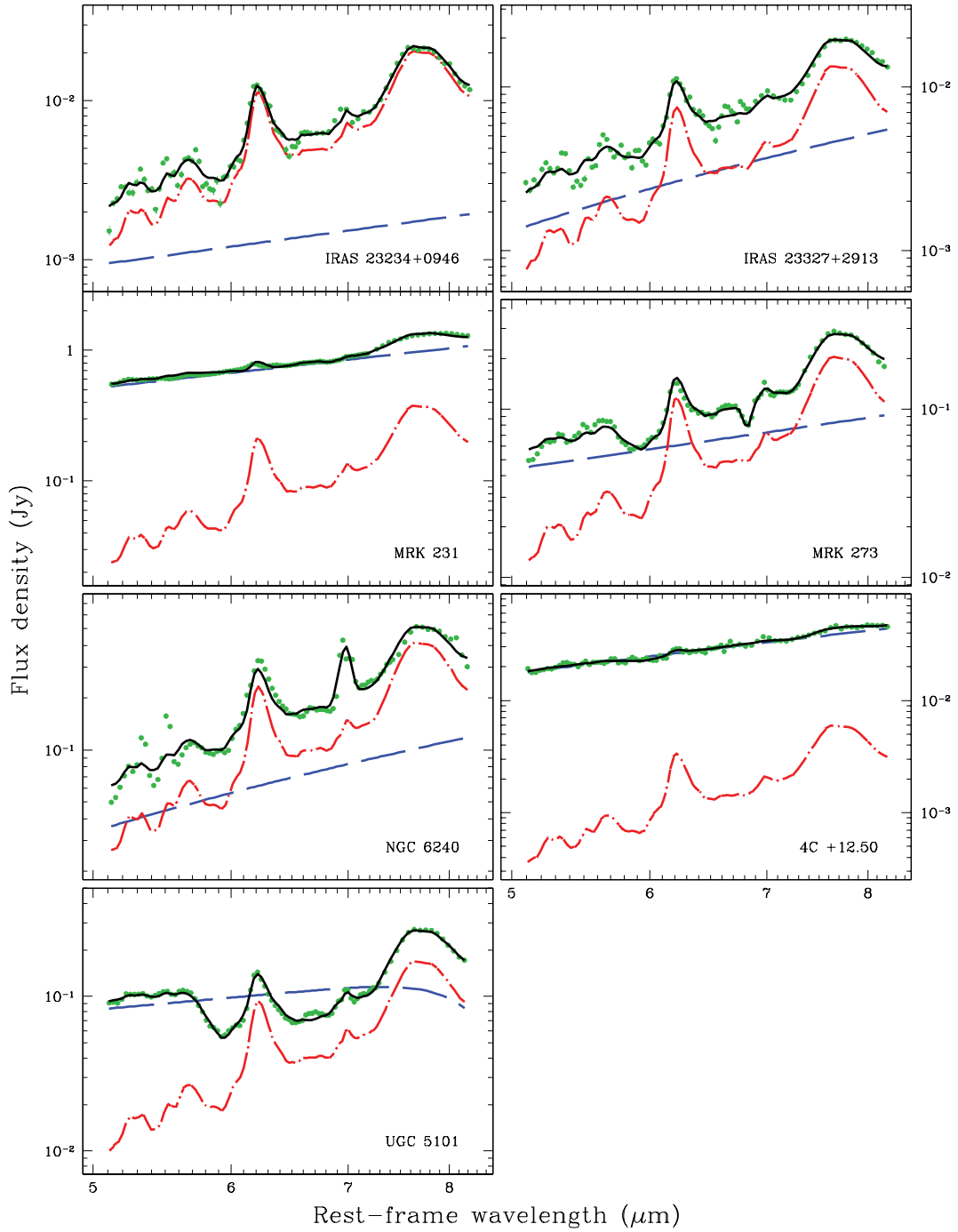
Figure A1 – *continued*

Figure A1 – *continued*

Figure A1 – *continued*

Figure A1 – *continued*

Table A1. Flux and equivalent width (with respect to the AGN component) of the 7.65 μm [Ne VI] fine-structure line. The uncertainties on both quantities range from ~5 to 30 per cent.

Source (IRAS)	[Ne VI] Flux (erg s^{-1} cm^{-2})	EW (μm)
04103−2838	1.0×10^{-13}	0.024
05189−2524	1.1×10^{-13}	0.008
12072−0444	2.3×10^{-14}	0.011
13454−2956	1.5×10^{-14}	0.040
17179+5444	3.8×10^{-14}	0.057

This paper has been typeset from a TEX/LATEX file prepared by the author.